applied sciences

MDPI

Review

A Review and Evaluation of the State of Art in Image-Based Solar Energy Forecasting: The Methodology and Technology Used

Carlos M. Travieso-González *, Fidel Cabrera-Quintero, Alejandro Piñán-Roescher and Sergio Celada-Bernal *

Digital Signal Processing Division, Institute for Technological Development and Innovation in Communications (IDeTIC), University of Las Palmas de Gran Canaria (ULPGC), 35017 Las Palmas de Gran Canaria, Spain; fidel.cabrera@ulpgc.es (F.C.-Q.); alejandro.pinan@ulpgc.es (A.P.-R.)

* Correspondence: carlos.travieso@ulpgc.es (C.M.T.-G.); sergio.celada@ulpgc.es (S.C.-B.); Tel.: +34-928-452-864 (C.M.T.-G.)

Abstract: The increasing penetration of solar energy into the grid has led to management difficulties that require high accuracy forecasting systems. New techniques and approaches are emerging worldwide every year to improve the accuracy of solar power forecasting models and reduce uncertainty in predictions. This article aims to evaluate and compare various solar power forecasting methods based on their characteristics and performance using imagery. To achieve this goal, this article presents an updated analysis of diverse research, which is classified in terms of the technologies and methodologies applied. This analysis distinguishes studies that use ground-based sensor measurements, satellite data processing, or all-sky camera images, as well as statistical regression approaches, artificial intelligence, numerical models, image processing, or a combination of these technologies and methods. Key findings include the superior accuracy of hybrid models that integrate multiple data sources and methodologies, and the promising potential of all-sky camera systems for very short-term forecasting due to their ability to capture rapid changes in cloud cover. Additionally, the evaluation of different error metrics highlights the importance of selecting appropriate benchmarks, such as the smart persistence model, to enhance forecast reliability. This review underscores the need for continued innovation and integration of advanced technologies to meet the challenges of solar energy forecasting.

Keywords: solar irradiance; nowcasting; all-sky camera; statistical method; regression method; satellite

Citation: Travieso-González, C.M.; Cabrera-Quintero, F.; Piñán-Roescher, A.; Celada-Bernal, S. A Review and Evaluation of the State of Art in Image-Based Solar Energy Forecasting: The Methodology and Technology Used. *Appl. Sci.* **2024**, *14*, 5605. https://doi.org/10.3390/app14135605

Academic Editor: Seung-Hoon Yoo

Received: 28 May 2024
Revised: 18 June 2024
Accepted: 20 June 2024
Published: 27 June 2024

1. Introduction

Today, weather forecasting is a crucial factor that must be taken into consideration when making logistics-related decisions across global, regional, and local scales. Accurate knowledge of future weather is essential in a wide range of economic activities, such as logistics, transportation, civil defense, resource management, aviation, agriculture, event planning, tourism, and industrial operations. As such, reliable weather forecasting is a vital element in many areas of modern life.

Despite the advancements in solar energy forecasting, several gaps remain in the current literature. One significant gap is the limited integration of diverse data sources, such as ground-based sensors, satellite images, and all-sky cameras, within a unified forecasting framework. Additionally, there is a lack of comprehensive evaluations that compare the performance of different forecasting methods using consistent metrics and benchmarks. Furthermore, existing reviews often overlook the potential of emerging technologies, such as artificial intelligence and advanced image processing techniques, in enhancing forecast accuracy. This review aims to address these gaps by providing a detailed comparative analysis of various forecasting methodologies and technologies, highlighting the benefits of integrated approaches, and offering insights into the latest advancements and their practical implications.

The energy sector has various meteorological service requirements to support decision-making processes, including day-to-day operations and long-term strategic planning. This makes logical sense given the complexity of the industry.

With the increasing share of solar power in the overall electricity grid, power plants face a difficult task trying to balance energy generation and consumption. This challenge is compounded by the ongoing promotion of sustainable and renewable energy sources by governments and organizations in response to the current energy crisis caused by excessive and uncontrolled fossil fuel consumption. To mitigate the negative effects of carbon dioxide emissions into the atmosphere, it is crucial for the energy sector to find innovative solutions to this problem.

Renewable power generation and usage, unlike fossil fuels, involves lower emissions; however, one disadvantage of renewable energy sources is their unstable nature [1].

The transient nature of renewable energy sources is exemplified by the supply fluctuations of solar energy caused by variable cloud conditions. To address this issue, recent research has explored the development of an irradiance-based weather derivative to hedge against cloud risk [2].

To use solar energy more efficiently, it is important for photovoltaic grid operators to have successful mechanisms that enable accurate, short-term forecasting of the amount of power produced by solar panels. Such forecasting is critical for the efficient scheduling and dispatch of distributed energy resources (DERs).

This report aims to address the issue of solar power forecasting by examining the evolution of techniques and technologies employed by various researchers. The studies reviewed are primarily focused on addressing the challenges and motivations previously mentioned.

Section 2 examines various radiation detectors used for forecasting solar irradiance. These detectors are classified based on the prediction time horizon they can cover. In Section 3, research developments in this field are presented based on different prediction methods employed. This includes a diverse range of approaches in detection algorithms and cloud segmentation and classification, as well as feature extraction and post-processing. Finally, Sections 4 and 5 provide discussions and conclusions resulting from the study conducted in the preceding sections.

The main focus of this paper is to discuss the innovation of very short-term spatial-temporal irradiance forecasting, including forecasting periods that are even shorter than the satellites' orbital period. To do so, this study utilizes various forecasting techniques that implement sky images captured from the Earth's surface via all-sky cameras.

To provide readers with a concise and visual summary of the progress made in this field, significant aspects, techniques, and achievements obtained from different studies are presented in a series of tables. These tables are conveniently summarized in Appendix A.

2. Review and Evaluation of Solar Irradiance Forecasting Sensors

To ensure a comprehensive and relevant review, we established specific inclusion and exclusion criteria for the selection of studies. The inclusion criteria were as follows:

- Studies published in peer-reviewed journals and conferences from 2000 to 2024.
- Research focusing on solar power forecasting using imagery-based methods, including ground-based sensors, satellite data, and all-sky cameras.
- Research that provides quantitative performance evaluations using standard error metrics.

The exclusion criteria included the following:

- Studies not available in English or Spanish.
- Papers that did not provide sufficient methodological details or performance metrics.
- Research focused solely on theoretical models without practical implementation or validation. These criteria ensured that the review covered a wide range of relevant and high-quality studies, providing a robust basis for the comparative analysis presented.

Solar irradiance forecasting systems can be broadly classified into three categories based on the technology used. The first category consists of sensor-based systems that

directly measure solar irradiance using pyranometers and pyrheliometers, or indirectly using photovoltaic systems, ceilometers, and temperature sensors. The second category comprises systems that process images taken from space, such as satellites, to make predictions. The third category includes systems that use all-sky cameras on the Earth's surface to capture images for prediction purposes.

Forecasting systems that predict solar irradiance are widely used in industries and plants that involve solar thermal and photovoltaic systems. These systems typically utilize satellite images and irradiance sensors to obtain data on global horizontal irradiance (GHI), direct normal irradiance (DNI), and diffuse horizontal irradiance (DHI).

However, the cost of acquiring satellite images and maintaining well-calibrated sensors is high. This is not only due to the required communication networks for data centralization and storage but also to the installation and maintenance of these sensors. Furthermore, these systems lack spatial-temporal resolution. Given these economic and technical limitations, the research and implementation of all-sky camera systems represent a promising opportunity.

The following sub-sections will review the research conducted and categorized by the different technologies mentioned above. A particular emphasis will be placed on the systematic aspect of all-sky cameras. A preceding section is also included to cover the most commonly used error metrics and persistence models. This will aid in demonstrating how researchers measure, quantify, and compare the quality of the forecasts performed.

2.1. Persistence Model and Error Metrics

The forecasting field commonly employs a benchmark for comparison based on the assumption that future conditions will remain unchanged over the forecast horizon. This assumption is known as the "persistence" model and serves as the basis for evaluating the performance of other forecasting methods. For instance, in solar irradiance forecasting, the persistence model assumes consistent future values for irradiance, power output, and the clear sky index (CSI/clearness index).

To compare two different models, such as the "persistence" model and the one studied, the forecast skill score, or *SS*, is calculated. The forecast skill score (*SS*) is a valuable metric for comparing the performance of two forecasting methods.

$$SS = \left(1 - \frac{\varepsilon_{prediction}}{\varepsilon_{persistence}}\right) \times 100\% \quad (1)$$

Therefore, to indicate the improvement or deterioration of their results compared to persistence or baseline models, many researchers utilize the *SS* to guide their conclusions. Nonetheless, caution should be exercised when comparing *SS* values between studies due to the large number of baseline models. Comparisons can only be made meaningfully when the persistence models agree on one of the persistence variables mentioned above.

To this end, it is worth noting a list of commonly used persistence models. One such model is the "naive persistence" model, which assumes that the future forecast will be identical to the last measured value. This model is particularly suitable for stationary time series with minor variations, such as when the expected weather conditions are like those of the previous day or when the forecast for the next hour is expected to be the same as the current measured value. Given these characteristics, such models are usually most appropriate for situations where little variation in observed patterns is anticipated.

For example, the persistence model used in [3], as reported in [4], is calculated using a clear sky model. On the other hand, the persistence model proposed by [5] predics that the solar energy will be equal to the last observation corrected by the clear sky index. The authors of [6], on the other hand, employs a clear sky index model based on extraterrestrial solar radiation. Meanwhile, Ref. [7] utilizes a two-day persistence model, where the forecast power output at each hour is the value of the power generated at the same hour two days earlier.

Given the non-stationary nature of solar irradiance time series, the naive persistence approach is often inadequate for intervals longer than one hour. To address this limitation, a new approach has emerged, which is applicable not only for longer time horizons but also for hourly intervals. Referred to as the "smart persistence" model, this method is reliable in situations where there is low variability and for short-term forecasting. It involves breaking down the solar power output into a stationary and a stochastic component. The stationary component is usually assigned to the clear sky index. The stochastic component is attributed to cloud-induced variations.

The method was first introduced by [8], where the stochastic component was incorporated into the power output. Since then, several authors have modified and implemented the model in different ways. For instance, Ref. [9] added a solar power index that depends on cloud cover, while [10] proposed a cloud speed persistence and ramp model to forecast power output and ramp events using endogenous measurements of cloud motion vectors. Similarly, Ref. [11] applied the smart persistence model, calculating the predicted photovoltaic (PV) power output as a function of the clear sky GHI irradiance derived from a Python package for solar power analysis. The method was also used by [12] when comparing their SolarNet model with the same persistence model based on a cloud cover index that they used in their previous research [13].

As demonstrated by the skill score (*SS*) equation, the performance of a forecasting model can be evaluated using various error metrics regardless of which persistence model is used for comparison.

Among these error metrics, the most used ones (ε) are Mean Bias Error (*MBE*), Mean Absolute Error (*MAE*), Root Mean Square Error (*RMSE*), and Standard Deviation (*STD*). These metrics were also employed in the studies reviewed above, where p_i is the predicted value, o_i is the observed or measured one, and N is the number of measured instants. Relative values are calculated for individual days and the observed mean daily measurement o_m is established as a reference.

- Mean Bias Error (*MBE*) is a metric appropriate for evaluating forecast bias by reflecting the difference between the average value and the actual value of measured magnitude. It is expected to be as small as possible.

$$MBE = \frac{1}{N} \cdot \sum_{i=1}^{N} p_i - o_i \tag{2}$$

$$Relative\ MBE = \frac{100\%}{o_m} \cdot MBE \tag{3}$$

- Mean Absolute Error (*MAE*) is a linear score which means that all individual differences are weighted equally in the average. It is a metric less sensitive to outliers than the widely used *RMSE* and is appropriate for estimating uniform prediction errors.

$$MAE = \frac{1}{N} \cdot \sum_{i=1}^{N} |p_i - o_i| \tag{4}$$

$$Relative\ MAE = \frac{100\%}{o_m} \cdot MAE \tag{5}$$

- Mean Absolute Percentage Error (*MAPE*) is used to evaluate uniform prediction errors such as *MAE*.

$$MAPE = \frac{100\%}{N} \cdot \sum_{i=1}^{N} \left(\frac{p_i - o_i}{o_i} \right) \tag{6}$$

- Root Mean Square Error (*RMSE*) measures the global error over the entire forecasting period.

$$RMSE = \sqrt{\sum_{i=1}^{N} \frac{(p_i - o_i)^2}{N}} \quad (7)$$

$$Relative\ RMSE = \frac{100\%}{o_m} \cdot RMSE \quad (8)$$

- Standard Deviation (*std* or *SDE*) is a relative measure of average dispersion that gives an idea of the magnitude outliers mentioned above.

$$std = \sqrt{\frac{1}{N-1} \cdot \sum_{i=1}^{N} ((p_i - o_i) - MBE)^2} \quad (9)$$

$$Relative\ std = \frac{100\%}{o_m} \cdot std \quad (10)$$

- Coefficient of determination (R^2) is one of the most common statistical metrics for characterizing model quality. It compares the error variance to the variance of the modeled data.

$$R^2 = 1 - \frac{var(p_i - o_i)}{var(o_i)} \quad (11)$$

- *KSI* aims to quantify the model's ability to reproduce observed statistical distributions.

$$KSI = \int_{x_{min}}^{x_{max}} D_n \cdot dx \quad (12)$$

where D_n is the difference between two cumulative distributions.

Regarding the above concepts, when the skill score is applied, such as in the case of *SS-MAE*, the performance of a model is compared to that of persistence in terms of Mean Absolute Error (*MAE*).

2.2. Measuring Sensors Used in Solar Irradiance Forecasting

As introduced earlier in this section, solar irradiance measuring sensors are often used in hybrid prediction systems where they serve as backup technology and/or validate data obtained from satellite, camera, or all-sky camera network images. However, the sensors used to measure weather variables and solar irradiance have an even greater impact when utilized as initial data inputs for numerical weather prediction (NWP), alongside radiosonde and meteorological satellite data. In these models, the system of differential equations is quite complex and can only be solved through laborious numerical methods. This is why it is known as numerical prediction. Additionally, the amount of data required for these models is enormous. These techniques were only developed with the advent of computers, and they only began to achieve a certain degree of accuracy when computing power significantly increased.

New studies are published every year with the aim of expanding the possibilities for predicting solar radiation. One of the most recent studies [14] presents new prediction models that use the latest available technology. Various studies demonstrate significant progress in improving the efficiency of solar production through the prediction of irradiation [15]. These results showcase the potential of solar forecasting methods to enhance the effectiveness of solar energy production. Several noteworthy authors have implemented direct measurement methods for weather variable forecasting. On one hand, Ref. [16] uses present values of mean daily solar irradiance and air temperature to predict solar irradiance for a 24 h horizon. Conversely, Ref. [17] utilizes adaptive linear models of solar power data from 21 rooftop PV systems to forecast values for every hour up to a horizon of 36 h.

In contrast, Ref. [18] takes irradiance values every 1 and 10 min from pyranometers located at different sites to forecast at 2 h resolution. Another study by [19] collects irradiance values from a weather station every 30 min and compares them to a set of profiles representing the energy patterns. In another approach, Ref. [20] recommends optimum locations for an irradiance sensor network to cover an area of 50 km × 50 km with a prediction frame of 30 s to 6 h. Another recommendation is including the use of an automated solar panel tracking system [21]. To obtain maximum solar energy, this system ensures that the solar panel is placed at a 90-degree angle to the sun's position.

Moreover, historical data from multiple sensor measurements such as irradiance [22–24], air temperature [24–26], aerosol optical depth (AOD) [27–29], or relative humidity [24,29] can be processed to predict solar energy output. By analyzing these historical measurements, clear patterns can be identified, leading to more accurate predictions.

As the need for improved solar collection technology becomes increasingly pressing, new methods for climate prediction are being developed. For example, one study [30] focuses on developing automated methods to estimate the spectrally resolved normal direct irradiance for solar energy applications. In another study [31], possible solutions to the problem of sensors in the shortwave regime (0.2–2.5 μm) are evaluated by simulating the spectral response to the standard AM 1.5 solar spectrum. These efforts demonstrate the ongoing commitment to advancing solar forecasting technology to improve the performance of solar energy systems.

The effect of feature selection on solar prediction is also a crucial consideration. In [32], learning models are applied to determine the significance of features in predicting direct normal irradiance (DNI) data. Understanding which features are most important can improve the accuracy and efficiency of solar irradiance forecasting models. To provide more versatile and efficient systems, the use of backup or validation technology is becoming more common in hybrid solar irradiance forecasting. In terms of solar irradiance forecasting, two main systems distinguish themselves: hybrid satellite-sensors and hybrid camera-sensors.

In the field of hybrid satellite-sensors, several publications can be highlighted. First, Ref. [33] proposes an ultra-short-term system that combines satellite imagery and weather information to support cloud motion predictions, specifically by means of wind data. However, Ref. [34] compares GHI forecasts at time horizons of 30, 60, 90, and 120 min, utilizing satellite imagery with the corresponding values measured by sensors at two different locations. The authors of [35] demonstrate that combining a forecast using an artificial neural network (ANN) model of ground-based data with satellite forecasts improves the global accuracy for few-hour forecasts. Conversely, Ref. [36] evaluated 110 days of satellite forecasts supported by ground-based measurements, specifically in San Diego, California. Additionally, Ref. [33] suggests an ultra-short-term GHI forecasting method by the combined use of weather information and cloud cover controlled through the satellite. The authors of [37] also contributed significantly by demonstrating that including satellite average albedos in ground-based data forecasting leads to satisfactory improvements.

The use of measuring sensors in all-sky camera systems is also widespread, like in the satellite case. For instance, one study [38] combines cloud cover forecasts of solar disc using cameras with real-time ground-based measurements to extract parameters for forecasts. Another study [39] applies 99 pyranometers distributed over an area from 10 km to 12 km to validate a 2-month set of images. In contrast, Ref. [40] uses a network of pyrheliometers, pyranometers, and a ceilometer at the Plataforma Solar de Almería in Spain to validate the results of DNI maps obtained by all-sky cameras. Recently, this study has been extended by the University of Oldenburg in Germany [41]. In addition, Ref. [42] uses historical power values from solar panels combined with sky images as input for their neural network. The authors of [43] place a pyranometer together with the cameras at each chosen location, while [44] employs pyranometers, pyrheliometers, and ceilometers, as well as weather stations at two energy centers in Newcastle and Canberra, Australia.

Sky cameras, along with computational algorithms, offer a promising approach to predict and mitigate the impact of cloud cover on solar irradiance, as discussed in [45].

Meanwhile, Ref. [46] provides insights into the factors influencing the performance of ANN-based prediction models. In [47], all-sky image feature extraction is used to derive regional and global weights, which are then integrated with a long short-term memory (LSTM) training model to estimate solar irradiance. Furthermore, Ref. [48] introduces a machine learning framework that leverages all-sky cameras and satellite observations to enhance intra-hour irradiance forecasting.

Finally, as mentioned above, NWP models make use of the extensive data volume gathered from various weather sensors and solar irradiance measurements. However, due to the sheer number of models available, this text focuses only on authors who have reviewed solar forecasting research based on the most widely used models [49,50]. These models include global-scale models like GFS (Global Forecast System) [51,52], medium-scale models such as ECMWF (European Centre for Medium-Range Weather Forecasts) [53,54], and small-scale models like MM5 (Mesoscale Model version 5) [18,55] and WRF (Weather Research and Forecasting) [56,57].

2.3. Satellites

In contrast to the NWP models discussed earlier, image processing enables substantially shorter-term horizon forecasts. Specifically, satellite imagery can be used for cloud detection and characterization to predict GHI with an accuracy of up to 6 h in advance [58].

One of the primary advantages of using satellites for data collection is their ability to capture large areas simultaneously, providing information on the spatial distribution of data. This allows for a more accurate representation of the spatial evolution of the data. With high spatial and temporal resolution, satellite imagery is an excellent data source for forecasting events that will occur several hours in advance. In addition to the previous section's studies, several research projects have utilized satellite weather measurements because of their higher spatial resolution in comparison to ground-based sensors. These measurements are used as an initial condition for NWP models [59–61] or are directly used for forecasting with shorter horizons than the models. For instance, one study [62] attained a higher resolution than ground-based measurements by using satellite radiation data, covering an area of 462 $\times$ 462 km with an approximate resolution of 11 $\times$ 11 km, represented by 1764 gridded cells, which is equivalent to 1764 GHI sensors.

Several publications have achieved higher spatial resolution for solar forecasting by utilizing satellite weather measurements, surpassing the resolution obtained with ground-based measurement stations. For example, one study [63] used MODIS spectroradiometer data from the TERRA satellite to derive land surface temperature (LST) and design an accurate predictor for spatial horizons at a regional scale in Queensland, Australia. Another study [64] utilized GHI measurements based on satellite data to test the predictive accuracy of long short-term memory (LSTM) models at 21 locations, 16 of which were in Europe and 5 in the USA. Additionally, another publication [65] predicted incident solar radiation (ISR) through the use of NASA's satellite spectroradiometer input data, including land surface temperature, cloud top pressure, cloud height, ozone, and water vapor, among others.

However, for the cloud monitoring provided by the imagery, much solar forecasting research relies on sky captures from high-resolution satellite imagery. For example, Ref. [66] proposes cloud motion estimations derived from Meteosat-9 cloud map images. Alternatively, Ref. [67] combines MVIRI (Meteosat Visible and InfraRed Imager) images with Meteosat satellite imagery (via the Heliosat model) to obtain the albedo calculations and predict the effect of clouds on insolation. Furthermore, Ref. [66] suggests two methods for extracting cloud motion vectors of daytime Meteosat-10 satellite imagery. Ref. [58], in contrast, utilizes the Himawari-7 satellite of the Japan Meteorological Agency (JMA) to forecast the cloud cover index by means of self-organizing maps (SOMs). Instead, Ref. [68] provides one of the few high-latitude predictive studies that have been conducted by using Meteosat Second Generation (MSG) Meteosat-11 imagery for forecasts of up to 4 h. Finally, for readers interested in using geostationary satellites for cloud analysis, there is a wealth of research available in this area, including a comprehensive review in one study [69].

Finally, regarding the geostationary satellite application, there are combinations of hybrid systems, less commonly used but equally valid as the ones mentioned above. For example, in Ref. [70], a generalized model for forecasting solar irradiance from 25 locations is explained by ground-based data extrapolated from a single location by means of satellite measurements and weather forecasts. Other studies have also investigated the combination of ground-based measurements, satellite measurements, and numerical models [35,61,71]

2.4. All-Sky Cameras

All-sky cameras have demonstrated high effectiveness in measuring relative sky radiance, and their potential continues to be revealed each year through new studies. One noteworthy example is a study that utilized multi-exposure techniques to showcase the capabilities of these cameras [72].

As previously discussed, solar irradiance forecasting has primarily focused on two approaches: physical models based on numerical methods for weather prediction (NWP) and direct prediction utilizing real-time satellite images for cloud cover forecasts. However, the limited resolution and uncertainty of initial conditions make NWP models invalid for cloud forecasts at specific locations and times [4,73]. While NWP can provide information days in advance, there are biases and random errors in irradiance predictions [74]. Various studies have reported on the limitations of these two approaches [10,75,76].

As mentioned earlier, all-sky cameras and satellites are primarily designed to predict cloud patterns and dynamics, and their generated images serve as a valuable tool for solar forecast research. While numerous studies have explored this aspect (as seen in reference [77]), the prediction resolution in both spatial and temporal domains has been significantly improved using a more cost-effective system. This system provides a resolution of a few kilometers, which is typically used in solar power plants, and a temporal resolution of a few minutes. Since irradiance variability for short-term horizons has a significant impact on solar power plants and, in turn, power systems, immediate prediction systems based on high-resolution sky images can offer direct irradiance forecasts to optimize the performance of solar power plants or solar farms, particularly in this scenario. These systems are usually based on high-resolution digital cameras equipped with fisheye lenses ("US6844991B2—Fisheye lens—Google Patents", 2005) and a dome for weather protection, see left part of Figure 1, as shown in the processing conducted in [78]. Hemispherical sky images are obtained (180° field of view to which the distortion produced by the lens is corrected [79–81] (see Figure 2)). In many cases, this is supported by pyranometers utilized for validating prediction models and shadow-bands to avoid a direct solar arc view [82–84].

These enhance the average life of the camera sensor but can significantly reduce cloud-tracking capability close to the sun; see the central part of Figure 2, which is the result of the segmentation carried out in [85]. Instead, in cameras without these shadow-bands, as direct sunlight is not blocked, the circumsolar region is influenced by glare effects resulting from direct focus and for specific angles of incidence, and thus, a scattering may be produced in the dome; see image of the all-sky camera associated to the left part of Figure 2. Otherwise, there are advantages to employing non-weather-specific cameras, such as easy installation, low cost, and no moving parts (solar tracker), with its corresponding apparition of robotic arms in the images.

A modality that also avoids the lenses is based on images obtained from a reflection of a convex mirror oriented to the sky [85–87] (see right part of Figure 2), which is also the result of the segmentation carried out in [83]. The mirror can be designed to correct lens distortion, which eliminates the need for software correction and corresponding computational savings [88].

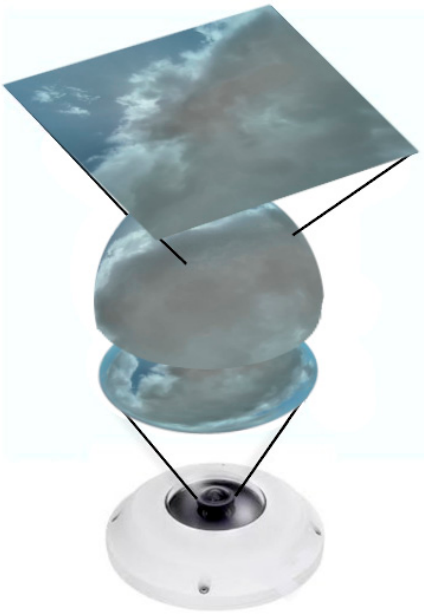

Figure 1. Distortion correction of fisheye lens.

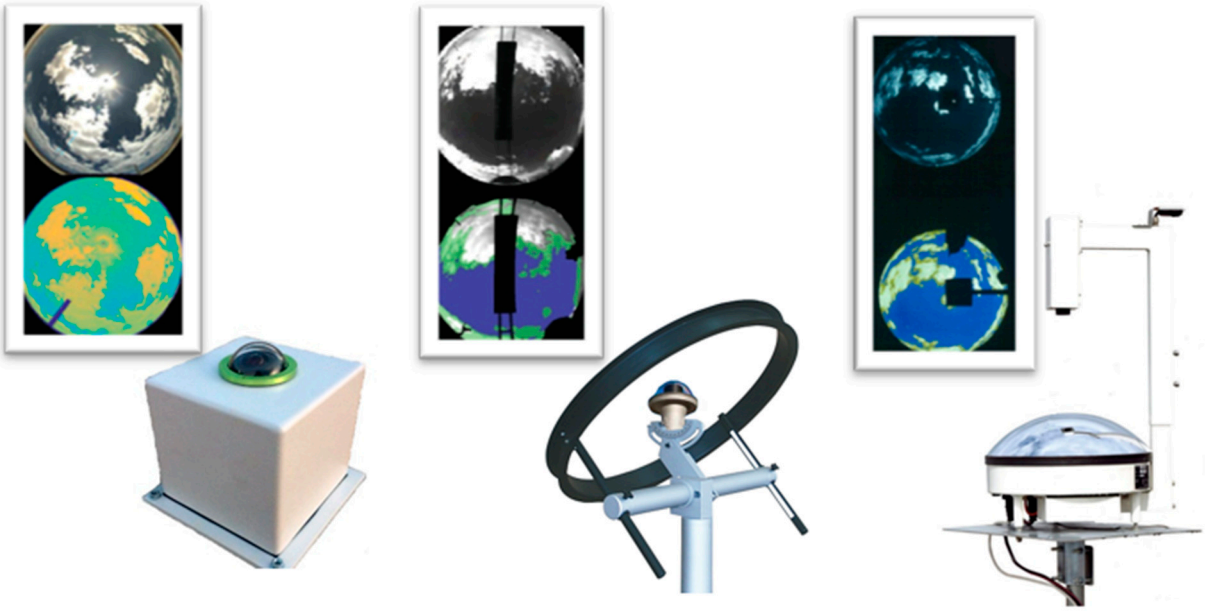

Figure 2. All-sky camera modalities and associated images. This figure presents various modalities of all-sky cameras, including examples of the images captured by each type.

Another option to avoid image saturation resulting from direct focus on the sun (without using a shadow disc or band) but require a more expensive infrastructure and more complicated maintenance are so-called shadow cameras. These are located on a mast sufficiently high to record a complete panoramic view of the solar power plant. The processing is now performed on images of solar irradiance maps, which are the result of shadows cast by clouds on the solar farm [78,89,90].

Ongoing research aims to optimize these novel predictive methodologies by developing higher-accuracy data acquisition systems that obtain local information from solar power plants. Two techniques have emerged in this context: the use of cameras that capture cloud images for very short-term forecasting, and irradiance sensor networks. However, the latter has a disadvantage, as it requires a large installation area for all the sensors to be sufficiently far from the solar farm to obtain accurate cloud cover forecasts with adequate separation

from each other. This prevents the redundancy of the obtained information. Unfortunately, locating large areas near a solar power plant for such a system can be unviable in many cases. Therefore, the use of cameras that capture cloud images provides a more feasible option for acquiring local data, improving the accuracy of solar power plant forecasts.

In contrast, it is possible to obtain an accurate characterization of the cloud cover at a given time and place with just a few cameras installed around a solar farm. Although to obtain three-dimensional estimations it is essential to utilize at least two cameras, despite this, it is still a lower-cost infrastructure in terms of investment and dimensions compared to sensor networks.

Regarding the spatial horizon that can be covered by solar forecasts, two types can be distinguished: Firstly, point forecasts, which predict solar occlusion by clouds and, therefore, only process forecasts for the camera location. Secondly, forecasts that calculate the height of the cloud base [91], an aspect that allows the cloud shadow projection on the ground to be deduced [92].

The total prediction area covered by these systems depends on the configuration in which the array of cameras is installed, typically ranging several kilometers.

However, a disadvantage of using a single camera is the inability to accurately characterize multi-layer cloudy sky conditions due to its limited 2D view [93,94]. In cases where the system is equipped with multiple cameras, methods have been developed to model clouds in three dimensions and account for up to four different heights.

In this regard, geolocation of clouds can be achieved by stereoscopic approaches [95] or via complementary remote sensors to calculate cloud heights (ceilometers [96,97]) [39,98,99].

Typically, the research that calculates cloud height via multi-camera systems aims to use this information to perform a cloud projection over a solar farm, i.e., so-called solar irradiance maps. For example, Ref. [40], spatially distributed four all-sky imagers to estimate predictions by means of individual 3D models for each cloud, extracting characteristics such as height, position, surface, volume, transmittance, motion vector, etc. The same author [98,100], a year later, downscaled the system to two 3 megapixel (MP) cameras to correlate height measurements with transmittance measurements of the clouds by employing pyrheliometers.

Alternatively, Ref. [101] separates 4 cameras at 500 m and 900 m distances from each other in order to produce sets of DNI maps every minute in a 30 km $\times$ 30 km region at a spatial resolution of up to 10 m. Meanwhile, Ref. [102] proposes a network of three cameras to provide sufficient coverage for a 32 MW photovoltaic solar power plant, which estimates the height and motion of each cloud layer based on the multiple images obtained. Moreover, Ref. [90] suggests a 4-camera system (WobaS-4cam, 3 MP and 6 MP) to obtain irradiance maps in a 50 MW solar field, which are evaluated with a shadow camera reference system.

In relation to single-camera systems, investigations commonly focus on cloud tracking and/or classification in order to predict the instant when the sun will be covered. For example, Ref. [94] utilizes a professional all-sky imager consisting of a camera (640 $\times$ 480 pixels) pointed at a spherical mirror (420 $\times$ 420 pixels) that reflects the sky image, by which it estimates future cloud motion. Alternatively, Ref. [44] uses one IP camera per site (Newcastle and Canberra, Australia) to predict the time period covered and its duration. Similar is the equipment used in [43] which, by employing two 3.1 MP cameras, one per site (Merced and Folsom), combines sky images with irradiance measurements to classify three future sky conditions: clear, cloudy, and partly cloudy.

In addition, Ref. [42] takes images from a 1280 $\times$ 1280 pixels camera at 180 m from a solar panel and with different exposition times (11,88,176,264 ms) to predict the short-term power output of the solar panel. Meanwhile, between 2016 and 2017, Cheng performed various studies [103–105] always utilizing a 640 $\times$ 480 pixels camera in conjunction with irradiance readings to forecast fast motion clouds, characteristic of a maritime climate, at the National Taiwan Central University. Finally, Ref. [42] uses images from a 2592 $\times$ 1744 pixels all-sky imager and 99 pyranometers distributed over 10 km $\times$ 12 km to predict different cloud scenarios. It is also very important to take into account the configuration of the

cameras. Recent studies have highlighted the importance of certain relevant aspects of all-sky cameras, such as their angular calibration, and how it impacts the results obtained [106]. Additionally, other studies have demonstrated the wide range of applications of this technology [107].

In order to analyze how many all-sky cameras have been used in the above-mentioned studies, Figure 3 has been developed showing the number of all-sky cameras used in each location. In this way, it will be possible to know in which areas these cameras are most used to carry out these investigations.

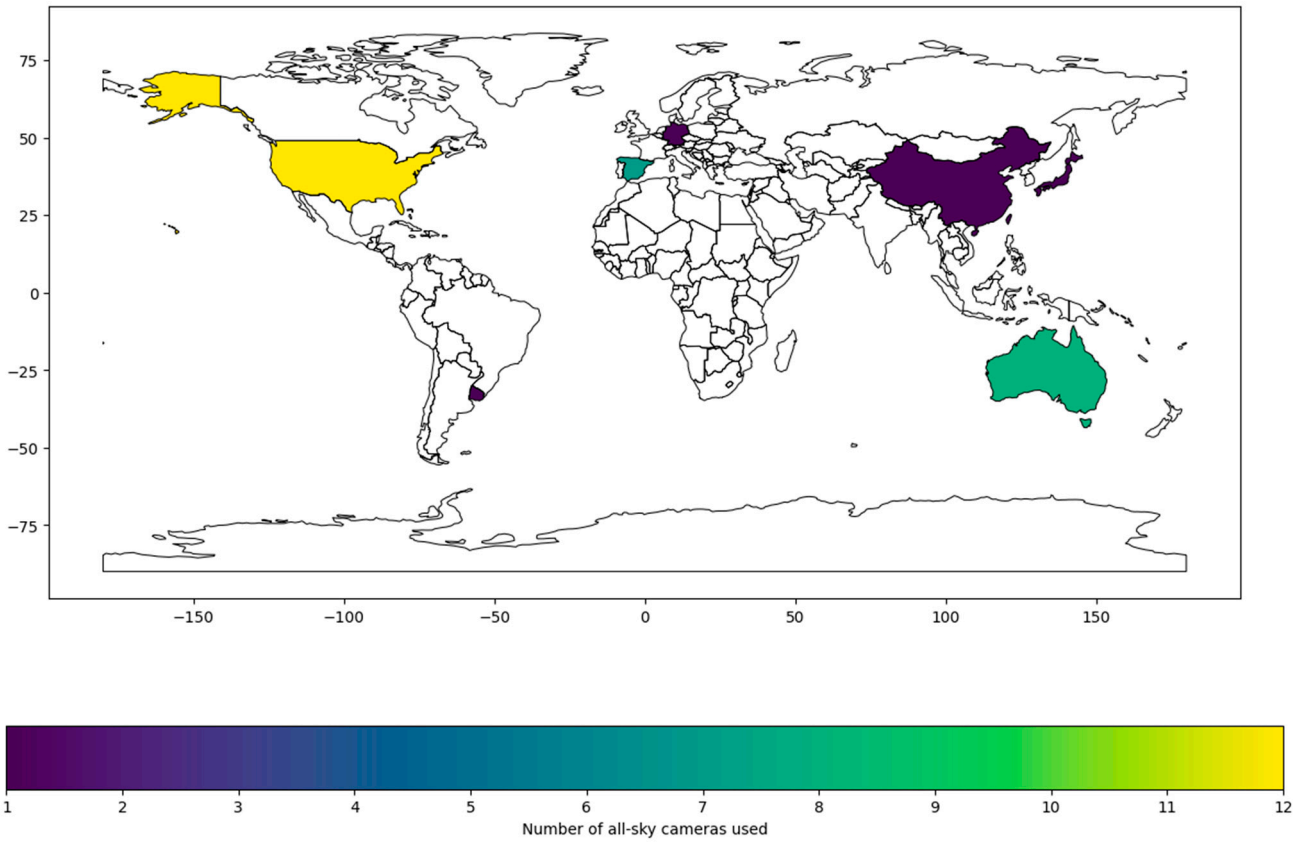

Figure 3. Number of all-sky cameras used in the surveys at each location. This bar chart displays the number of all-sky cameras deployed across various geographic locations for survey purposes. Each bar represents a location and the number of cameras used, providing insight into the distribution and extent of survey coverage.

To expand upon the investigations cited in this section, Table A1 is included in Appendix A, which details each of the studies, the objectives set, as well as the type of data used for it, and the final results obtained, which, in turn, are measured and compared with certain models and specified error metrics. Table A1 includes only the research that innovates with a solar irradiance predictive model (excluding research that is limited to evaluating and comparing models), or those studies involving concepts that support the subject of this article, such as, for example, those concerning the distortion correction of fisheye, the amount of aerosol in the atmosphere, or cloud profiles.

In order to analyze the location of the solar forecasting studies shown in Table A1, Figure 4 has been developed. This figure shows a map indicating the number of studies carried out at each location. In this way, we can know how many studies have been developed in different locations.

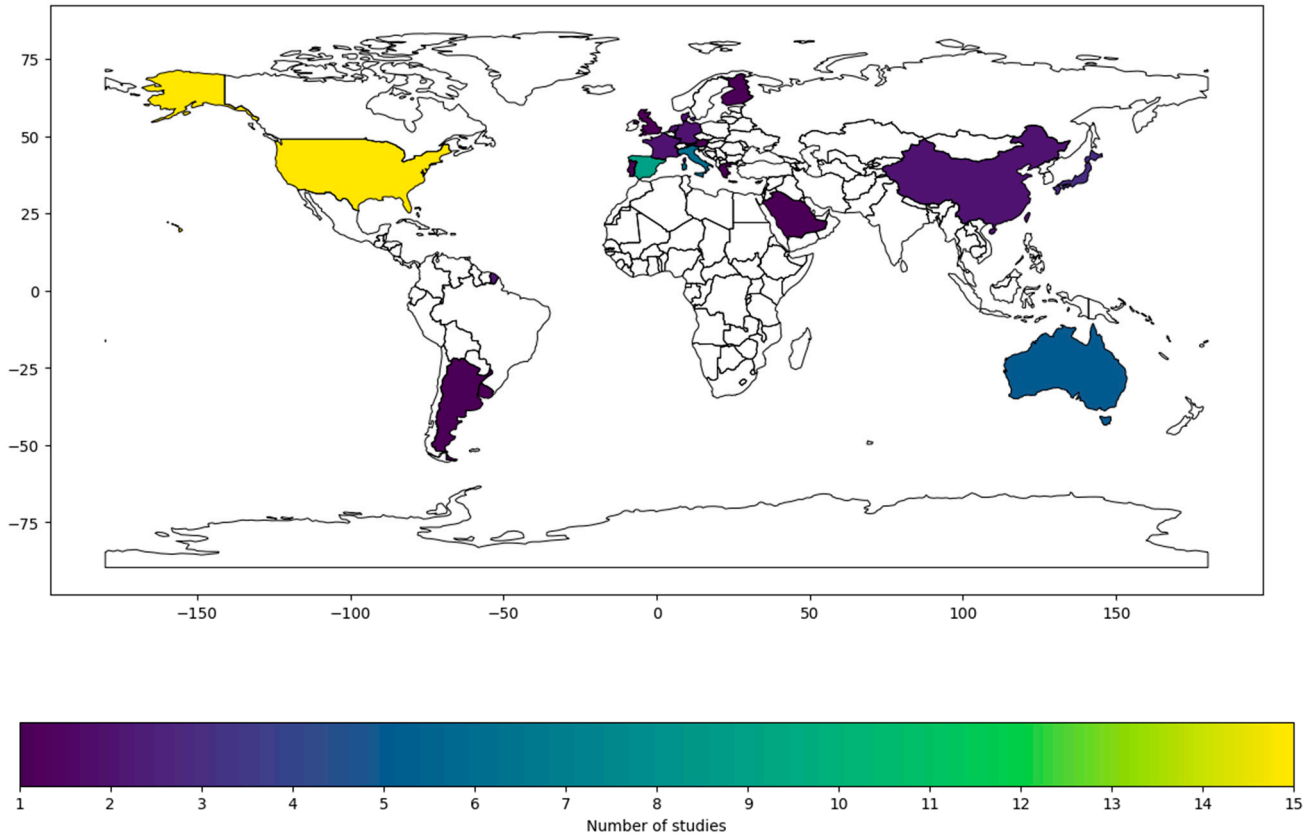

Figure 4. The number of studies carried out at each location. This figure shows the number of studies conducted at different locations, presented as a bar chart. The data indicate the intensity of research activity at each site, offering a comparative view of research focus areas.

3. Review and Evaluation of Solar Irradiance Forecasting Methods

This section presents a study of various research studies that have utilized the technology explained earlier, categorized based on the methodology employed to obtain solar irradiance forecasting.

To ensure a comprehensive and relevant review, we established specific inclusion and exclusion criteria for the selection of studies. The inclusion criteria were as follows:

- Studies published in peer-reviewed journals and conferences from 2000 to 2024.
- Studies employing advanced methodologies such as statistical regression, artificial intelligence, numerical models, and image processing techniques.
- Research that provides quantitative performance evaluations using standard error metrics.

Exclusion criteria included the following:

- Studies not available in English or Spanish.
- Papers that did not provide sufficient methodological details or performance metrics.
- Research focused solely on theoretical models without practical implementation or validation. These criteria ensured that the review covered a wide range of relevant and high-quality studies, providing a robust basis for the comparative analysis presented.

The complexity of physical processes involved in atmospheric dynamics and the interaction of solar radiation with the atmosphere has hindered the development of a single, universal model for solar irradiance forecasting. The various physical factors that influence the solar irradiance received, particularly cloud conditions, make it necessary to differentiate between models. Solar forecasting techniques can be classified into three main categories based on the input data utilized: NWP-based models, statistical and machine learning techniques, and image-based methods. Hybrid methods that incorporate elements from each of these categories and apply various techniques can also be included within

this classification. The NWP-based methods are well accepted for a spatial resolution of between 10 and 100 km^2 [108] and forecasts 6 h ahead; thereby at six to seven days the real accuracy is already estimated to be only 60% [109].

On the other hand, statistical and machine learning models use historical data to perform deep learning of features, particularly atmospheric features. The training model then provides forecasts based on new values of the input variables, making these models applicable for a wide range of temporal and spatial horizons, being utilized mostly in hourly forecasting studies. Meanwhile, image-based methods, as discussed in the previous section, employ all-sky cameras, shadow cameras, or satellite imagery mainly for cloud segmentation and tracking. Shadow cameras are suitable for intra-hour forecasting and a spatial resolution of a few to hundreds of meters, while satellite-based methods are advantageous for a forecast horizon varying from 30 min to 6 h and a spatial resolution of about 1 km^2 [110]. This classification is summarized in a forecast classification by time horizon, in which the nowcasting, short-term forecasts, and forecasting techniques are differentiated and illustrated in Figure 5.

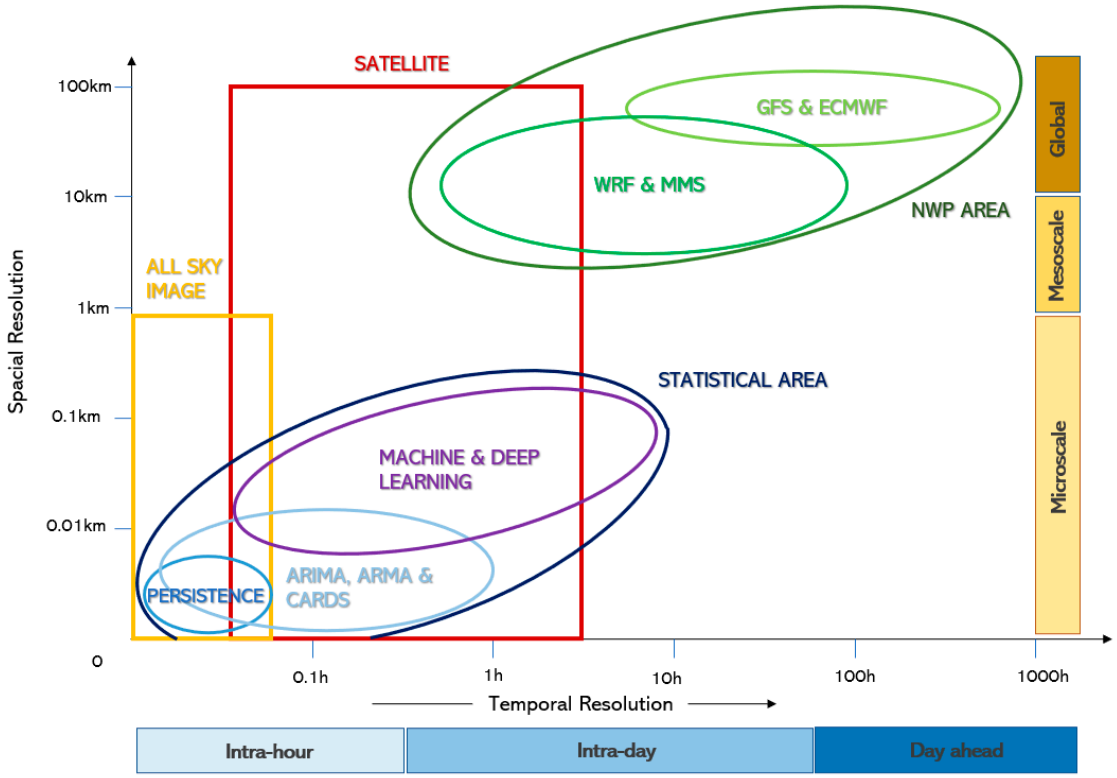

Figure 5. Forecast method classification by spatio-time horizon. This figure categorizes various forecast methods according to their spatial and temporal horizons. It provides a clear framework for understanding the different types of forecasting techniques, ranging from short-term to long-term forecasts, and their spatial scopes.

In this section, the approaches presented in the literature for each of the aforementioned techniques will be reviewed, as well as the researchers who have combined them to create hybrid models. Moreover, the nowcasting technique using ground-based cameras, specifically all-sky cameras, through image processing will be evaluated in more depth, building on the previous section.

3.1. Statistical Methods

Statistical methods rely on data to extract associations from historical data and predict future behaviors. Therefore, the accuracy of the forecast depends on the reliability of the historical data. Selecting a suitable training dataset is a crucial factor in achieving accuracy

in the developed model. Additionally, a large historical dataset is typically required because these methods benefit from the ability to correct errors associated with imprecise input data measurements [111].

There are two distinct approaches based on historical solar irradiance data. The first approach involves regression methods that statistically analyze time series data, while the second approach involves non-linear artificial intelligence (AI) methods.

3.1.1. Regression Methods

This set of techniques tries to find the association between a dependent variable (GHI, DNI, DHI solar generated power, etc.) and independent variables (predictors), based on statistical analysis. Depending on a time series treatment, different techniques can be applied: stationary or non-stationary, linear or non-linear. The most relevant techniques studied by researchers are the following:

Stationary linear models. Studies based on these models usually propose approaches using autoregressive models AR (regress the dependent variable on lags of itself in time period t), or derived more generic models, such as the ARMA autoregressive moving average model (historical values are considered as errors) [37,112], ARX models (AR with exogenous inputs) [17] or its adaptation VARX (vector ARX) [113], and the ARMAX model (ARMA with exogenous variables) [114].

Non-stationary linear models. In the analysis of a non-stationary time series, the main ones are as follows: the autoregressive integrated moving average model ARIMA (using data variances and regressions) and SARIMA (Seasonal ARIMA) [115], in which a seasonal component is introduced [116].

Stationary non-linear models. These can be obtained mainly by means of the Non-linear Autoregressive Models with Moving Average and Exogenous Input (NARMAX) model, which achieves unbiased estimates in the presence of non-linear noise [117].

3.1.2. AI Artificial Intelligence Techniques

AI techniques have generated a great deal of interest in solar irradiance forecasting research due to their breakthroughs in optimization, pattern recognition, and classification. The most used AI techniques in irradiance forecasting are as follows:

Artificial neural networks (ANNs). These are the most widely used machine learning techniques in solar power forecasting. The most common are MLPs, multi-layer perceptron structures, but due to the large number of topologies, it seems appropriate to propose only publications that review the solar forecasting techniques by the ANN, for example, [118–120].

k-Nearest neighbors (k-NN). It is one of the simplest machine learning methods; thus, for renewable energy forecasts, the prediction about future outcomes is based on historical data with a similar time of day and weather conditions.

Deep learning (DL). Compared to traditional machine learning approaches, DL can perform feature extraction by itself and the improvement of learning performance is proportional to the dataset increase; therefore, it properly solves situations involving a large amount of data and hence, it is an effective technique in weather prediction. Various DL techniques can be highlighted in the field of solar forecasting, such as the restricted Boltzmann machine (RBM), deep belief network (DBNs), the automatic encoder AE, its stacked version (SAE), LSTM networks, stacked LSTM networks and convolutional neural networks (CNNs) and deep convolutional neural networks (DCNNs). For readers interested in this field, there are studies available that compare deep learning (DL) techniques for solar irradiance forecasting. Some examples of such investigations are in [121–123].

Mycielski graph-based models are used for prediction. In [124] a Mycielski-based model is proposed which considers the hourly recorded solar radiation data as a matrix and, starting from the last recorded value, tries to find the most similar submatrix pattern in history.

Support vector machines (SVMs). Compared to the k-NN, SVMs operates effectively with small sample sizes while the k-NN is more sensitive to the size increase in the training dataset [125].

Random forest (RF). This has been widely used in many prediction fields due to its high tolerance to low information and improved fitting ability [126].

Markov chains. Normally utilized in hybrid systems, they has been widely used to generate sequences of the solar irradiance data, as well as to predict the daily global solar irradiance data by combining typically with neural networks [127].

Coupled autoregressive and dynamical system (CARDS). This model has been used in the literature for probabilistic predictions based exclusively on endogenous data. This model is characterized by decomposing GHI as the sum of a cyclic term and an autoregressive term [128–131].

Numerous studies have investigated the effectiveness of combining or comparing different techniques in a hybrid system. Research studies such as [131,132] have compared machine learning models with AR models, demonstrating the potential benefits of hybrid systems in forecasting and prediction tasks. In addition, Ref. [133] developed a forecasting model for solar power generation by combining ARMA with ARIMA. These studies illustrate the diverse range of techniques utilized to forecast solar radiation and highlight the potential benefits of utilizing a combination of techniques for enhanced accuracy and reliability.

Different approaches have been proposed for solar irradiance forecasting, including data-driven methods and Markov switching models. For instance, Ref. [134] applies data-driven approaches such as the boosted regression tree (BRT), ANNs, and SVM boosted regression trees, as well as benchmarks with the AR and ARX models.

Meanwhile, Ref. [135] presents the comparison of Adaptive Neuro Fuzzy Inference System (ANFIS) and Autoregressive Moving Average with eXogenous term (ARMAX) in forecasting global solar radiation.

Wavelet neural networks (WNNs). WNNs have improved generalization properties compared to ANNs, making them more suitable for modeling high-frequency signals such as local transients and intermittency [136–138].

Ref. [139] presents a solar irradiance forecasting method for remote microgrids based on the Markov switching model to schedule the energy resources in these microgrids. Moreover, Ref. [140] proposes a robust deep learning approach based on an automatic encoder-triggered recurrent unit (AE-GRU) for short-term solar energy forecasting. These various techniques can potentially enhance the accuracy and reliability of solar irradiance forecasting, highlighting the need to explore and compare different methods to improve the performance of such systems.

In contrast, several research studies have employed machine learning or deep learning techniques, either independently or in combination with some of the techniques previously discussed. This is due to the vast amount of data that needs to be processed. These approaches demonstrate the versatility and adaptability of these techniques in managing large and complex datasets for accurate solar radiation forecasting. A prime example is [141], which suggests a convolutional long short-term memory (CLSTM) system that combines a deep learning convolutional neural network CNN with an LSTM network. Following this line, in [142], a spatio-temporally bound deep network based on CNNs and LSTM is proposed and in [143], a spatio-temporal solar radiation prediction model based on a convolutional graph network and LSTM is proposed.

For instance, Ref. [144] designs a model in which the deep neural network (DNN) uses the reconstructed values estimated by four LSTM models with temperature data and statistical characteristics to predict PV power values. Ref. [145] uses a CNN-assisted deep echo state network that uses multiple time-scale dynamic learning repositories to generate short-term solar power forecasts. However, Ref. [146] associates the deep learning algorithms such as DBN and AE with LSTM to compare forecasts of a standard MLP in 21 solar power plants. Ref. [147] evaluates four scenarios (long window, short window, a

Principal Component Analysis (PCA), and a clear sky model) with three typical forecast horizons by means of an irradiance database combined with the information measurements and an extreme learning machine (ELM).

However, Ref. [148] follows feature extraction with a convolutional autoencoder and a K-means clustering algorithm compares and analyses the results with CNN, LSTM, and ANN models. Ref. [42], instead, compares MLP, CNN, and LSTM models using historical photovoltaic power values and sky images as the input. Ref. [149] proposes a deep CNN with a hybrid data input composed of sky images and PV panel output data.

In addition, there are studies that propose innovative hybrid approaches to predict global solar radiation (GSR). For instance, Ref. [150] introduces a new 4-phase hybrid CXGBRFR framework that combines a deep learning convolutional neural network, extreme gradient boosting with random forest regression, and a Harris Hawks optimization for initial function selection. Similarly, Ref. [151] compares several AI-based alternatives, including MLP, Random Forest Regressor, and Gradient Boosted Trees, to predict cloud shadow locations over solar panels. These studies showcase the continued efforts to develop and improve hybrid approaches that leverage the strengths of different techniques to enhance solar radiation forecasting.

In general terms, the common methodology of research utilizing machine learning and deep learning coincides with that illustrated in Figure 6.

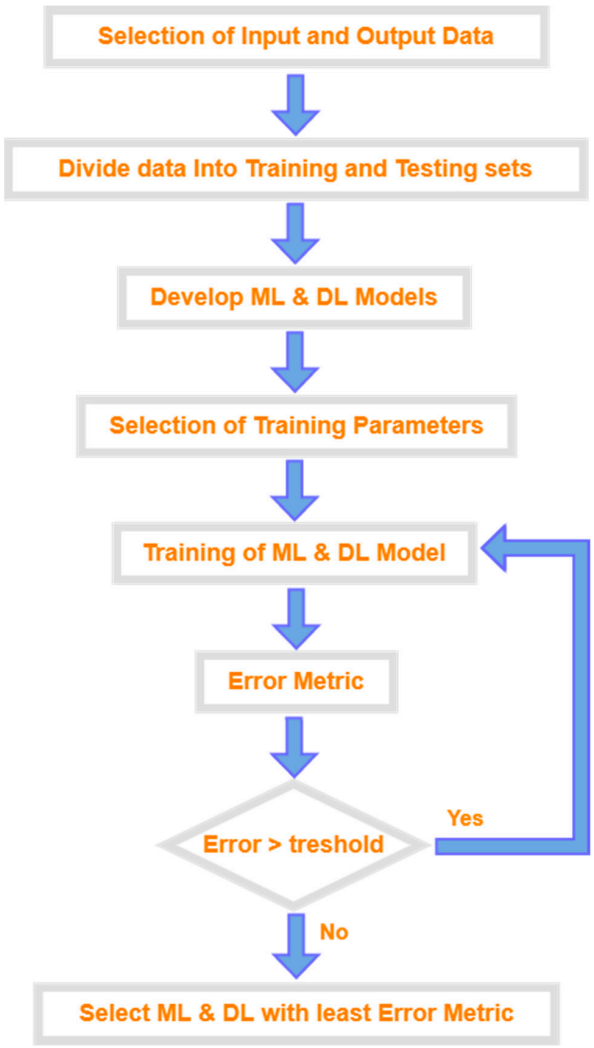

Figure 6. ML-DL methodology. This figure outlines the machine learning and deep learning methodology employed in the study.

To conclude, publications comparing and evaluating AI techniques for solar forecasting are also provided [152–155].

3.2. Numerical Models

Ground-based pyranometer stations cannot provide full coverage, and traditional statistical models based on time series have limited applicability, making numerical weather predictions (NWPs) a viable alternative on a global, regional, and national scale. NWP involves modeling the temporal development of the atmospheric state using differential equations that describe the physical laws of climate. Data from radiosondes, meteorological satellites, and ground-based meteorological observations are utilized for this purpose. These observations are processed using data assimilation and analysis methods, which perform quality control to obtain values that can be used by the mathematical algorithms of numerical models. These algorithms are typically based on a uniform spacing grid. The resulting data are then used as a starting point for forecasting. The set of equations used in NWP are known as the primitive equations.

In terms of size and grid spacing, numerical weather prediction models are typically differentiated by their spatial scale. Additionally, a variety of methodologies are employed in the development of these models, resulting in a multitude of different models. Some noteworthy global and regional models include the Global Forecast System (GFS), the National Oceanic and Atmospheric Administration (NOAA), and the European Centre for Medium-Range Weather Forecasts (ECMWF). Mesoscale models such as MM5 and WRF are also widely used.

Irradiance forecasts vary in their models, with differences in data assimilation techniques (such as 3D-Var, 4D-Var, and EnKF), the number of vertical layers of the atmosphere handled, consideration of concentration values for aerosol, H_2O, O_2, O_3, and CO_2, the number of parameterizations for different physical processes, and the degree of sophistication of scattering/absorption schemes used, as well as the number of updates per day and loop time steps. Independently of the spatial resolution that different methods may provide, the solar forecasting research that is exclusively based on numerical models generally performs this when searching for forecasts at a time horizon longer than 6 h, whereas, if the aim of the study is a shorter forecast, the numerical methods are applied as backup systems to improve accuracy.

There are a number of studies that utilize forecasts provided by various numerical models to evaluate the effectiveness of different forecasting methods. For instance, Ref. [156] shows the importance of developing a seasonal and site-specific model output statistics (MOS) approach to improve forecast accuracy in the evaluation of the GHI forecasts from the WRF model in southern Nevada. In addition, Ref. [157] evaluates the irradiance forecast accuracy at time horizons of about 24 h from the ECMWF model and demonstrates that NWP forecasts can be an essential tool for the operation of solar power generation systems. The same author of [53] goes on to describe the use of various post-processing methods, especially multivariate regression models, in numerical ECMWF forecasting for day-ahead forecasts. Moreover, Ref. [158] analyses performance improvement by incorporating hourly aerosol estimates into the ECMWF model, while Ref. [159] proposes a method to forecast the GHI and DNI up to 6 h in advance by inserting the Meteosat Second Generation (MSG) cloud index estimates into the vertical layer of the WRF model.

On the other hand, there are several studies that use numerical models as a verification or backup system for other methods. For instance, Ref. [160] supports the use of a stochastic differential equation model with an NWP for modeling the uncertainty associated with a GHI forecast. Similarly, Ref. [161] establishes a methodology to shorten the 24 h forecasts provided by the WRF model through an ANN technique. Ref. [162] combines three implementations of the WRF model with multivariate statistical learning techniques.

Alternatively, other studies present an approach for short-term solar irradiance forecasting based on the Physical Solar Model (PSM) v3 in combination with machine learning models. For example, Ref. [49] suggests a hybrid forecast based on gradient-boosting re-

gression and bootstrap aggregation machine learning models. Similarly, Ref. [163] proposes a hybrid forecast based on the GB gradient boosting method, but in this case, it utilizes the GFS model. Additionally, Ref. [121] evaluates their PV forecasting method with processed historical data using three different mesoscale, global, and regional numerical models (North American Mesoscale (NAM), GFS, Short Range Ensemble Forecast (SREF)).

In contrast, Ref. [164] proposes a corrective algorithm to improve the GHI forecasts given by the ECMWF using ANNs. Ref. [165] presents a hybrid forecast model (Hybrid WT-PSO-SVM) that combines wavelet transform, particle swarm optimization, and the SVM with the data from numerical models such as COSMO, WRF, RAMS, and MM5.

Several studies compare numerical models with each other to assess their accuracy and reliability. For example, Ref. [166] analyzes three leading models in Australia, namely GFS, the Australian Community Climate and Earth-System Simulator (ACCESS), and ECMWF Reanalysis v5 (ERA5). Ref. [167] evaluates models such as SolarAnywhere, ECMWF, GFS, high-resolution rapid refresh (HRRR), and the national digital forecast database (NDFD), as well as satellite-based cloud motion.

3.3. Image-Based Methods

As introduced in the preceding section, the numerical prediction models have the potential to provide forecasts by simulated clouds at high spatial and temporal resolutions. However, the forecast performance during the first 12–24 h is influenced significantly by the cloud analysis accuracy and initial thermodynamic conditions. Due to non-linear cloud processes and their associated effects on radiation, the numerical models tend to underestimate low clouds (typically stratus clouds and coastal regions) and, therefore, lose accuracy in the solar irradiance forecasting at the surface [168].

Accurately predicting the extent, motion, formation, dissipation, and transmittance of constantly changing clouds is a complex and unrealistic task for solar forecasting applications on medium time scales. Cloud condition imagery, captured through satellites, imagers, or all-sky cameras, offers excellent data for short-term forecasting or nowcasting due to its high spatial and temporal resolution. This type of imagery is particularly useful for improving the control of the significant impact that clouds have on the solar irradiance reaching the Earth's surface. When compared to numerical models or time-series forecasting, cloud condition imagery is a superior source of data for accurately predicting the immediate effects of clouds on solar irradiance. Solar irradiance forecasting models based on image processing commonly utilize two techniques: the clear sky index and cloud motion vectors. The application of motion vector fields directly on the cloud cover coefficient allows for the accurate prediction of solar irradiance forecasts from images. By combining these two methods, solar irradiance forecasting models can more accurately predict changes in solar irradiance caused by cloud movements.

The following sections will present a review of research that utilizes sky imagery, regardless of whether the traditional method mentioned above is followed. The studies will be logically differentiated between those that use satellites as an image source and those that employ cameras to take images from the surface.

3.3.1. Satellite Imagery

From a quantitative perspective, a satellite image is a measurement of the radiance emitted or reflected by the Earth–atmosphere system, integrated over a specific wavelength range, time instant, and spatial window. For solar irradiance forecasting, the most commonly used satellite imagery includes thermal infrared images, water vapor-based cloud coverage images, and visible light spectrum images that capture surface albedo and cloud reflection. These images provide a wide range of analyses, containing valuable information for predicting solar irradiance.

This includes cloud characterization, as well as other factors that influence the forecast such as wind direction and the Earth's surface albedo. In terms of cloud appearance and shape, geostationary satellite imagery provides information on cloud amount, shape,

and thickness. Additionally, AMV (Atmospheric Motion Vector) images offer insight into atmospheric motion, including wind direction and speed in the lower, middle, and upper wind fields. Furthermore, satellite irradiance imagery is of particular interest in the field of solar energy; these are based on the amount of reflected light intensity from the ground, and thus irradiance can be combined with module temperature to forecast photovoltaic power generation [169].

In this regard, researchers who use satellite imagery as input data typically utilize one or more of the aforementioned types of imagery. As an example, Ref. [170] developed a short-term forecasting model for solar irradiance ramps by generating irradiance maps through the projection of cloud maps obtained from satellite imagery. The model then estimates the evolution of the moving cloud projection based on wind data from NWP (numerical weather prediction) models. In contrast, Ref. [68] creates a GHI forecast model by combining information from the clear sky model of Pvlib Solis with consecutive images from the geostationary meteorological satellite by applying the Heliosat method. Ref. [171] develops a GHI and DNI forecast algorithm by deriving cloud motion vectors and utilizing the clouds' physical properties through infrared and visible spectrum imagery. Ref. [172] presents a prediction model based on deep neural networks to predict the amount of solar energy potential using geostationary satellite image data in units of one hour for more than 7 years. Ref. [34] introduces a GHI forecasting approach based on satellite observations and ANN networks; thus, the satellite images that are processed via the algorithms for velocimetry and cloud indexing are utilized as inputs to the ANN model.

In comparison, Ref. [173] estimates the three radiation components using MSG satellite imagery and the Heliosat-2 model and achieves this by calculating the attenuation for any sky condition and the present estimated value compared to the value of the previous 15 min. However, Ref. [58] provides a study in which they designed an (ELM) extreme learning machine model to forecast the incident solar radiation (ISR) by means of extracted data from the imaging spectroradiometer satellite and applied this to 41 uniformly distributed locations. Ref. [174] developed a solar irradiance mapping model that utilizes feature importance analysis to calculate terrestrial solar irradiance using only satellite data. In a similar vein, Ref. [175] employs satellite imagery in their forecasting algorithm by testing various variables, such as the clear sky index Kc, the solar zenith angle (SZA), the surrounding cloud pattern, and North Atlantic weather regimes as predictors.

Moreover, several publications have compared satellite results with those provided by regional-scale numerical models, as seen in [176] in Korea. Additionally, some studies have compared satellite results with those obtained from ground station measurements, such as [70], which compared results at 25 locations in the Netherlands, and [177], which employed Meteosat East for comparison.

3.3.2. All-Sky Images

To obtain a forecast with higher temporal resolution than that provided by satellites, statistical techniques such as time series analysis or neural networks can be applied to radiometric measurements on the surface or motion vector techniques on all-sky camera measurements. This is necessary as global model information is not available for these time horizons.

When investigating all-sky cameras, both mirrored and non-mirrored as well as shadow disc or non-shadow disc configurations often face a common initial challenge: cloud characterization. Clouds can scatter and absorb radiation, which affects radiation attenuation. The degree of attenuation depends on cloud micro- and macro-physical properties, making it difficult to accurately segment and classify clouds for estimating cloud attenuation when the sun passes over them. Therefore, this task is not a trivial endeavor [178].

Moreover, investigations can obtain cloud detection and tracking from all-sky imaging information. In fact, some authors even classify and characterize clouds to improve the accuracy of predicting the degree of occlusion as they pass through the solar disc.

Cloud segmentation in all-sky images is a critical task for any forecasting system. However, it is a complex task due to the variability of color and intensity caused by a range of factors. These include different cloud types and layers, sun positions, aerosol interference (e.g., pollution, dust), as well as saturation and glare effects in the circumsolar region. To characterize aerosols, the Linke turbidity is calculated based on direct normal irradiance (DNI) or global horizontal irradiance (GHI) measurements using the Linke turbidity model [179].

To overcome the challenges of cloud characterization, researchers have made efforts to improve the accuracy of cloud segmentation and classification. Various approaches have been proposed in the literature, such as using neural networks, correlation between RGB (Red Green Blue) or RBR (red–blue ratio) channels, and SVM classifiers. These approaches have been validated and discussed extensively in the literature.

Cloud detection and segmentation algorithms have traditionally relied on fixed thresholds applied to RGB values of images [180–188], the red–blue ratio (RBR) [42,43,46,47,104], or comparisons with clear sky libraries (CSLs) [108,189,190]. While this approach performs well in most conditions, difficulties arise in cases of very dark clouds and foggy conditions near the sun. Accuracy is also limited when the color temperature of the sky changes significantly, such as near sunrise and sunset [44]. To address these challenges and reduce reliance on fixed thresholds, machine learning approaches were developed [191–193], as well as adaptive threshold methods such as MCE (Minimum Cross Entropy) based on Otsu's algorithm [194].

The MCE classification algorithm was developed and tested in [187] as part of an HYTA (hybrid thresholding algorithm). The MCE algorithm selects a threshold by minimizing cross-entropy between the original and segmented image, generating a robust and unbiased method for image histograms. Ref. [34] also utilized the MCE method and concluded that the threshold value must be limited within an estimated interval of the training set. After determining the threshold, pixels with an RBR higher than this threshold are classified as cloudy. Building on these studies, Ref. [43] developed a hybrid system that combines the MCE method with the FTM (fixed threshold method) and the CSL (clear sky library). The study uses the FTM and MCE method for cloud detection and the CSL to address image glare.

The CSL method is a database of clear sky images for the different solar zenith angles. It is widely applied to remove the geometric variation of clear sky RBR values that depend on the sun pixel angle and zenith angle. This is achieved by subtracting or compensating the RBR of the input image by the CSL RBR reference corresponding to the same zenith angle [195]. Very typically, for cloudy images, the pixels in the circumsolar region are incorrectly identified as sky pixels due to this CSL compensation. In order to account for this effect, the Haze Correction Factor (HCF) is iteratively used to correct the images before applying the cloud identification [188,196].

The FTM method is one of the fixed threshold methods for the RGB values introduced above. It is based on the fact that cloud pixels have higher red intensity (R) values than sky pixels [43]. In general terms, the segmentation is more manageable for single-layer clouds, and preferably for optically thick cumulus clouds, low turbidity, and high solar elevations, due to the high contrast. Instead, optically thin clouds are a considerable challenge for all the segmentation approaches.

An illustrative example of results from the correction processing, segmentation, and motion vector generation is presented in Figure 7 by using the results presented [43].

When low solar elevation and a high Linke turbidity factor occur simultaneously, the blue color of the sky becomes low in saturation and appears as a whitish-grey color. Segmentation in these conditions becomes challenging even for a human observer, as only partially illuminated clouds contrast enough with aerosol layers to be distinguishable from each other [40]. Several studies have discussed the reduced boundary between clouds and aerosols in such cases [197–199]. Cloud classification is a valuable task for researchers due

to several reasons. For instance, it can help identify different cloud types, detect vertical growth, and determine if multiple layers are present within a cloud.

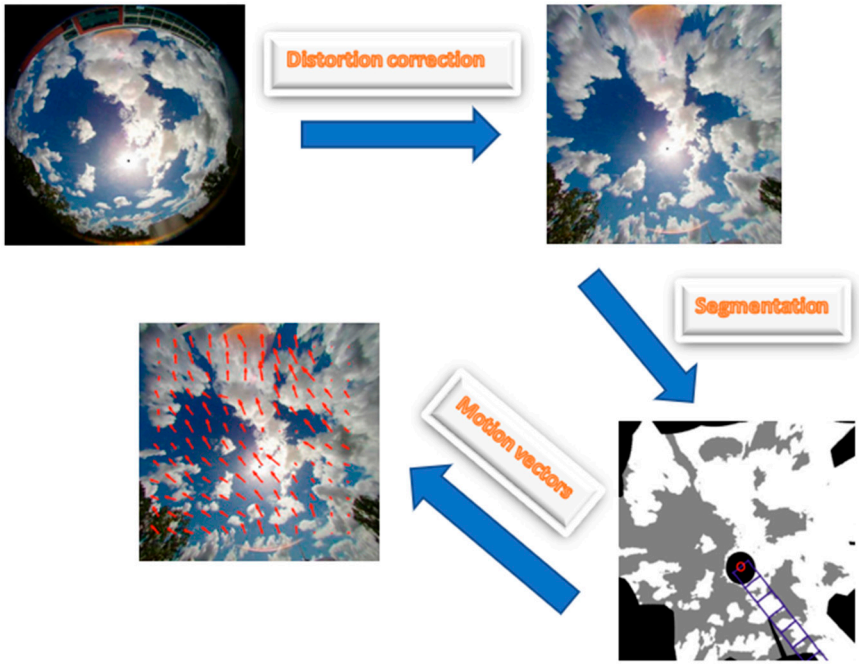

Figure 7. An example of the segmentation and generation of motion vectors. This figure demonstrates the process of segmentation and the generation of motion vectors. It illustrates how images are segmented and how motion vectors are created, which are essential for analyzing dynamic changes in the observed scene.

On one hand, the vertical cloud profiles contain important information for the different cloud types [190,191]. Clouds can be classified into different types based on their height in the atmosphere. The troposphere, the lowest layer of the atmosphere, is typically divided into three levels: lower, middle, and higher.

Some clouds, such as nimbostratus (Ns) and deep convective clouds, may extend over multiple layers of the troposphere. The boundary between layers is not static and can vary depending on the latitude of the planet, as well as where a cloud is located. As such, some authors divide the planet into three latitude belts: polar, mid-latitude, and tropical. Each belt has its own associated interlayer boundaries [200].

In [201] the accuracy of the cloud height measurements with two layers, derived from the Atmospheric Infrared Sounder (AIRS), is investigated and measured over a period of five days of observations.

Cumulus (Cu), stratus (St), and stratocumulus (Sc) clouds are associated with the lower level of the troposphere. These clouds are typically low-lying and can cover large areas. Altocumulus (Ac) and altostratus (As) clouds are associated with the middle level of the troposphere and are typically found at higher altitudes than lower-level clouds. Cirrus (Ci), cirrocumulus (Cc), and cirrostratus (Cs) clouds are associated with the higher level of the troposphere and are typically found at very high altitudes. These clouds are thin and often appear wispy or feather-like [202].

Conversely, the optical properties of clouds play an essential role in determining their impact on the atmosphere's radiation budget. Clouds have distinct optical properties that can vary depending on factors such as the size and shape of cloud particles, water content, and vertical extent. These distinct properties describe different attenuation degrees, mainly due to the absorption and scattering that occurs in the cloud [203].

The attenuation caused by the clouds is described by the cloud optical thickness (COT), which depends on the micro- and macro-physical properties of a cloud. These properties include particle size distribution, shape, water path (WP), thermodynamic phase, and

vertical extent [190]. In [204] modern methods of passive remote sensing of water and ice clouds are discussed.

The water path (WP) of a cloud is a crucial parameter in determining its COT. The WP describes the vertically integrated water content (WC) and effective particle size of a cloud [205]. In particular, low- and mid-layer clouds generally have a considerably larger global WP than high-layer clouds, making the WP parameter especially significant in understanding the optical properties of clouds. Furthermore, the effective particle size of a cloud is also an important factor, as a larger particle size leads to higher absorption, while a smaller particle size increases scattering [206].

Current cloud detection and classification methodologies vary depending on the research aim. A review of the current cloud detection and classification methodologies is provided by [207]. In most cases, researchers can fine-tune the degree of cloud classification to fit within their parameters. For example, many investigations that aim to predict occlusion-type or ramp-down-type events in a solar farm generally use a simpler cloud classification system. This system may only distinguish between cloud and no-cloud types [103–105] or may use categories such as clear, partly cloudy, and cloudy [49–51].

An occlusion event occurs when the sun is covered or obscured by clouds when they move into the sun's location in the sky. In contrast, ramp-down events occur when the irradiance drops drastically in a short time interval. Both events can be predicted using cloud tracking and clustering data and are critical in solar power forecast scenarios. If the predicted solar power is not sufficient to be delivered to the utility, the PV operator may need to initialize alternative energy sources. As such, it is clear that these events can have a significant impact on solar power generation and the overall efficiency of solar farms.

In contrast to the simpler cloud classification discussed above, studies that aim to predict the attenuation levels more accurately focus on a deeper classification of cloud type. Various research exemplifies these deeper and more complex cloud-type classifications. Several studies classify clouds and conditions into three distinct classification groups. Ref. [208], for example, distinguished cirriform, cumuliform, and waveform clouds with a 90.97% accuracy rate via infrared images. A similar classification case can be seen in [209]. This study used an SVM and a BPNN (back propagation neural network) to classify three cloud conditions per pixel.

Alternatively, clouds may be classified into four groups. For instance, Ref. [82], divided clouds into four types based on their transmittance index. Likewise, Ref. [191] opted to unify several cloud types into four groups to avoid incorrect classifications and achieved satisfactory results with various classifiers, such as using an MLP (multi-layer perceptron) and an SVM (Support Vector Machine). These several cloud types were based on the cloud classification published by WMO in 1987 (WMO, 1987). However, it should be noted that the accuracy in this study was reduced when cirrus clouds appeared. This decrease in accuracy is due to the cloud's thin parts, which are easily confused with clear skies, and in other cases, to the brightening effect of the regions around the solar disc.

There are some studies that divide clouds into even more complex groups. Ref. [210] utilized five different feature extraction methods in an automatic training classification system to recognize cumulus, towering cumulus, cumulonimbus, clear sky, and other clouds. In this study, autocorrelation, cooccurrence matrices, edge frequency, Law's features, and primitive length were used. Ref. [181] extends the classification from five groups to seven cloud types by means of the k-NN (k-nearest neighbor) classification algorithm. This algorithm is best for recognizing clear sky conditions and cirrus clouds. It is found in Heinle's study that the most confusing causes for inaccuracy are low-cloudy conditions (lower than 30%) and the glare effect of the circumsolar region. To improve the classification of seven cloud types proposed by Heinle, Ref. [39] applied an SVC support vector classifier. Moreover, Ref. [184] highlights Heinle's seven cloud classification model, detecting these types successfully in 78 to 95% of the cases.

Finally, Ref. [211] references up to eleven cloud types at high resolution. For such numerous classifications, the main issues arise from three cloud types: stratocumulus

with altostratus, cirrostratus, and stratus clouds. This complication is due to a mutual transformation between the three cloud types. Despite this, the same classification is also proposed by [39]. This study achieved an accuracy of 92% after a ten-fold cross-validation. However, the accuracy is low for cirrus and cirrostratus clouds as the RBR threshold is not able to distinguish properly.

After cloud segmentation and classification, the velocity and direction of cloud motion are typically determined using a cross-correlation method (CCM) applied to two consecutive sky images. This method identifies the movement of a block of pixels between two images by finding the region in the second image that has the highest correlation with each block of the first image. The resulting motion vector grid contains information about the observed motion direction and velocity. However, cloud formation, deformation, and evaporation can occur during the process. When this occurs, the correlation is reduced considerably, even though the assumption of spatial homogeneity of cloud velocities is made. Additionally, the appearance of clouds can change over time due to variations in white balance settings, cloud illumination, and different viewing geometries [108].

Several approaches have been proposed to monitor cloud formation and deformation during cloud motion. For instance, Ref. [212] used a non-rigid structure to model the complex dynamics of cloud motion, achieving a 19% improvement over the rigid technique presented in [108]. In fact, the study utilized optical flow techniques, specifically the Thirions Demons algorithm [213] and the variational approach of [214].

In contrast, Ref. [215] showed that common computer vision techniques, such as the Lucas–Kanade algorithm [216] and optical flow, perform better for cloud tracking in cases of low pixel displacement between successive images. In Ref. [217], a deep learning-based cloud detection and classification algorithm was developed for advanced Himawari image measurements (AHI) from the Himawari-8 geostationary satellite. Additionally, Ref. [218] incorporated an IPSI-based multi-transform-fusion (MTF) method to improve accuracy in cloud motion displacement (CMD) calculations and [219] propose a forecasting method based on a phase correlation algorithm for motion estimation between subsequent cloud maps derived from Meteosat-9 images.

To conclude, Table A2, found in Appendix A, outlines visually the works discussed in this section to provide detailed information on the investigations carried out. As in Table A1, Table A2 excludes those studies that concentrate on evaluating and comparing previous models or those that focus on additional aspects from the main subject of this article.

4. Discussion

As noted throughout the text, the specific method or technology selected by researchers depends on the required forecast time. The all-sky cameras and regression methods have demonstrated a notable performance for the very short forecast time of up to one hour. In comparison, methods based on weather satellite imagery have been found to be more optimal for a time scale of up to 6 h. However, for a time scale of several hours, cloud dissipation and formation start to interfere with the methods' dynamics and growth. As such, in these cases, the cloud tracking methods are no longer comparable in accuracy to the numerical weather prediction models (NWP). The NWP models, in turn, start to decline at time horizons of several days. A major question that plagues solar forecasting research is the type of camera used for sky images. As shown, there are many types of cameras that can be used for solar forecasting. Some of the most common variants are professional imagers, cameras that record the reflection of a convex mirror oriented to the sky, shadow cameras, and conventional high-resolution cameras (usually security IP).

As mentioned in Section 2, all-sky imagers are considerably more expensive than conventional cameras. In fact, all-sky imagers are more prepared for extreme weather conditions and have heating/ventilation for fog, condensation, and snow. Additionally, these cameras, as well as the cameras with a convex mirror, often have a solar tracking device to cover the solar disk. Though at an extra cost, this coverage extends the average life of the camera sensor and avoids possible image glare. Similarly, in terms of costs,

shadow cameras require expensive masts. These masts are expensive because they must be sufficiently high enough to capture the shadows cast by clouds to be monitored on the surface.

As such, in terms of cost, conventional high-resolution cameras are significantly easier to acquire. One advantage of using these cameras is that they do not record the robotic arms of the solar shading system, making it easier to track clouds as they pass through this area. However, when using this type of camera, the circum-solar regions of the images will appear saturated by the solar glare effect on the sensor. Furthermore, conventional high-resolution cameras will not be able to resolve the inclemency of adverse weather or seasonal conditions.

Despite the drawbacks of using this type of camera, many researchers opt for using conventional high-resolution cameras to perform predictive studies. This is mainly due to their relative affordability and accessibility. Indeed, judging from the results analyzed in this article, the majority have been successful and comparable to the results obtained from studies applying more technologically sophisticated methods.

Nevertheless, in terms of the sustainable generation of power, the assessment of hardware costs shows that all-sky cameras are more affordable than other technologies discussed in Section 2. Figure 1 highlights the effectiveness of combining all-sky cameras, satellites, and measuring sensors for nowcasting forecasts.

Consequently, all-sky cameras are more appropriate for use in solar farms. Indeed, a solar farm requires cameras that have good spatio-temporal resolution and a sensor network of well-calibrated pyranometers and pyrheliometers to cover a typical total area ranging from hundreds of meters to a few kilometers. Considering the cost of satellite image acquisition and the implementation of such sensor networks, all-sky cameras are the most economical choice.

Figure 3 shows the distribution of all-sky camera surveys conducted. All-sky cameras are mainly deployed in countries with high technological development, such as the United States and Australia, which lead to investment and the use of this technology. Adoption is more incipient in regions between the subtropics, such as Uruguay, where the availability of resources and infrastructure limits their implementation. In Asia, China and Japan are increasing their camera monitoring capacity, although not at the same level as the United States and Australia. In Europe, countries such as Spain have also developed numerous studies using all-sky cameras, indicating greater coverage than initially reported. Coverage remains uneven globally, with limited representation in Africa and parts of South America, suggesting the need for international cooperation for a more equitable distribution of this advanced technology.

Throughout the review of the various techniques and associated measuring instruments, it has been emphasized that characterizing the complexity of the atmosphere as accurately as possible requires a significant amount of data. Regarding the validation of results in different studies within this context, it is important to consider the impact that the validation period. As reported in the literature, the validation period may have an impact on the methods and outcomes.

For instance, in techniques involving large amounts of data, such as numerical models or deep learning methods, the results' validation period is presupposed to be optimal. Conversely, in the image processing models, for example, those conducted via satellite or ground-based cameras, the validation must reflect all possible weather scenarios as far out as possible. This process means that if the validation period is short for any reason, the value of the conclusions may be unrealistic.

Apart from the spatial-temporal resolution differences previously discussed between all-sky cameras and satellites, it is worth noting that the resolution of geostationary observations from satellites decreases at higher latitudes due to the high satellite zenith angle. This causes the estimation of global horizontal irradiance (GHI) to become increasingly challenging as the pixel size is stretched by the curvature of the Earth. This limitation is demonstrated in conjunction with the high variability of sunshine hours at high latitudes

in research such as that of [61] in Finland. Another remarkable constraint in the satellite image processing is the albedo of snowy surfaces, which is like certain clouds and can cause confusion in the irradiance images.

Logically, the image assessment from the Earth's surface also has associated critical circumstances that are not present in the satellite space situation. Upon reviewing the studies that employ all-sky cameras in Section 3, it is apparent that those which integrated cloud classification in their research faced certain challenges. This is especially true when dealing with conditions of low or very thin clouds and in skies with a high aerosol concentration. These types of circumstances induced confusion between the pixels corresponding to the sky and those corresponding to the clouds.

To provide a clear and concise overview, in Table 1, we present an analysis of the sensors and methods summarizing their strengths and weaknesses:

Table 1. Critical analysis of solar energy forecasting sensors/methods.

Forecasting Sensors/Method	Strengths	Weaknesses
Ground-Based Sensor Measurements	• High temporal resolution. • Effective for very short-term forecasting. • Real-time data.	• Limited spatial coverage. • High maintenance and calibration costs.
Satellite Data Processing	• Extensive spatial coverage. • Suitable for medium to long-term forecasts.	• Lower temporal resolution. • Susceptibility to cloud cover and atmospheric conditions. • High data processing costs.
All-Sky Camera Images	• High-resolution images. • Enables very short-term forecasts. • Real-time detection of cloud cover.	• Limited to camera coverage area. • High initial setup costs. • Reduced accuracy in adverse weather conditions.
Statistical Regression Approaches	• Simple implementation. • Effective trend identification with historical data.	• Heavy reliance on historical data quality. • Limited adaptability to sudden weather changes.
Artificial Intelligence (AI) Methods	• Handles large datasets. • Identifies complex patterns. • Accuracy improves over time.	• High computational resource requirements. • Need for specialized expertise and potential opacity in decision-making process.
Numerical Models	• Detailed atmospheric simulations. • Robust for medium to long-term predictions.	• Computationally intensive. • Accuracy depends on initial conditions and model resolution.
Hybrid Methods	• Combines multiple data sources. • Enhances accuracy. • Reduces uncertainties.	• Complex integration. • High computational demands. • Requires multi-disciplinary expertise.

This review has identified several emerging trends and novel approaches in solar energy forecasting that hold promise for improving forecast accuracy and reliability. One significant trend is the increasing use of artificial intelligence and machine learning techniques, which can analyze large datasets and identify complex patterns that traditional methods might miss, leading to more accurate and adaptive forecasts. Additionally, the development of hybrid models, which combine various forecasting methods such as

ground-based sensors, satellite data, and all-sky cameras with AI and numerical models, shows potential for reducing uncertainties and enhancing forecast robustness. Advanced image processing techniques, particularly those utilizing deep learning algorithms, are improving the interpretation of satellite and all-sky camera images, enabling more precise detection of cloud movements and other atmospheric phenomena affecting solar irradiance. The incorporation of real-time data assimilation techniques, which continuously update forecasting models with the latest observational data, also enhances short-term forecast accuracy by capturing sudden changes in weather conditions. Furthermore, the deployment of Internet of Things (IoT) devices and extensive sensor networks is providing high-resolution, real-time data across larger spatial areas, facilitating more localized predictions. Lastly, blockchain technology is emerging as a secure and transparent method for managing and sharing forecasting data, enhancing data integrity, facilitating collaboration among stakeholders, and ensuring the reliability of data used in forecasting models. These trends represent significant advancements in the field of solar energy forecasting, and their continued development and integration into existing systems are expected to address current limitations and drive further improvements in forecast accuracy and reliability.

Finally, the distribution of studies by country, shown in Figure 4, indicates that research activity is most intense in the United States and several European nations, with a notable presence also in China, Japan, and Australia. The distribution of studies is uneven globally, with lower representation in Africa and parts of South America. This suggests the need to improve infrastructure and funding in under-represented regions to encourage more globally balanced research.

5. Conclusions

This article provides an updated review of the techniques and technologies related to solar forecasting research. More specifically, this article focuses on the very short-range forecasting method that utilizes sky imagery captured by all-sky cameras from the Earth's surface. Indeed, this method offers significant potential for further research in the field of stabilization and optimization in the photovoltaic solar power sector. The article compares the different approaches for solar forecasting in terms of the forecasting method, technologies employed, spatio-temporal horizons to be covered, the measurement error, and the benchmark model. The various modalities of techniques are classified according to their methodological and technological fields. Their respective advantages and disadvantages are also examined.

In order to provide a comprehensive assessment, research methods based on irradiance measuring sensors are evaluated separately from those employing satellite and all-sky camera techniques. Additionally, a distinction is made between investigations that employ statistical and deep learning methods versus those that use numerical models. Another differentiation is made as well as with those utilizing satellite images or ground-based cameras. Furthermore, comparisons are drawn between studies that utilize a combination of these techniques and the instrumentation in hybrid systems.

In terms of equipment, the current high-resolution cameras are low-cost, offer high temporal and spatial resolution, and are effective for short-range irradiance forecasting compared to satellite images. They require less infrastructure, making them promising solutions for addressing the current imbalance in solar power generation by accurately predicting future PV generation outage events.

While there are many techniques available and the forecasting results are encouraging, there are still areas for improvement. Difficulties that continue to plague the field of solar forecasting are mainly due to clouds. Techniques for processing thin clouds such as fog, handling cloudy skies, dissolution, formation from other clouds, and dealing with cases of multi-layer clouds still need to be better developed. In such cases, hybrid systems have shown significant advances. Nonetheless, there is a lack of articles that calculate cloud height by stereoscopic methods to project cloud shadows on the surface and provide irradiance maps. Therefore, the future of solar forecasting lies in combined approaches

that control the non-linearity of cloud processes, refine accuracy by correctly estimating background errors, and ultimately contribute to optimal solar power generation. In the end, advancing such approaches will alleviate the current energy crisis.

Author Contributions: Conceptualization, C.M.T.-G., F.C.-Q., A.P.-R. and S.C.-B.; methodology, C.M.T.-G., F.C.-Q., A.P.-R. and S.C.-B.; software, C.M.T.-G., F.C.-Q., A.P.-R. and S.C.-B.; validation, C.M.T.-G., F.C.-Q., A.P.-R. and S.C.-B.; formal analysis, C.M.T.-G., F.C.-Q., A.P.-R. and S.C.-B.; investigation, C.M.T.-G., F.C.-Q., A.P.-R. and S.C.-B.; resources, C.M.T.-G., F.C.-Q., A.P.-R. and S.C.-B.; data curation, C.M.T.-G., F.C.-Q., A.P.-R. and S.C.-B.; writing—original draft preparation, C.M.T.-G., F.C.-Q., A.P.-R. and S.C.-B.; writing—review and editing, C.M.T.-G., F.C.-Q., A.P.-R. and S.C.-B.; visualization, C.M.T.-G., F.C.-Q., A.P.-R. and S.C.-B.; supervision, C.M.T.-G., F.C.-Q., A.P.-R. and S.C.-B.; project administration, C.M.T.-G., F.C.-Q., A.P.-R. and S.C.-B.; funding acquisition, C.M.T.-G., F.C.-Q., A.P.-R. and S.C.-B. All authors have read and agreed to the published version of the manuscript.

Funding: This research received no external funding.

Data Availability Statement: No new data were created or analyzed in this study. Data sharing is not applicable to this article.

Acknowledgments: This work is supported under Grant CEI2021-06, from direct agreement SD-21/08 by Consejería de Economía, Industria, comercio y conocimiento from Gobierno de Canarias to ULPGC.

Conflicts of Interest: The authors declare no conflicts of interest.

Abbreviations

ACCESS	Australian Community Climate and Earth-System Simulator
AE	Automatic Encoder
AI	Artificial Intelligence
AMV	Atmospheric Motion Vector
ANFIS	Adaptive Neuro Fuzzy Inference System
ANN	Artificial Neural Network
AOD	Aerosol Optical Depth
ARIMA	Autoregressive Integrated Moving Average
ARMA	Autoregressive Moving Average
ARMAX	Autoregressive Moving Average with Exogenous Variables
ARX	Autoregressive with exogenous inputs
BPNN	Back Propagation Neural Network
BRT	Boosted Regression Trees
CARDS	Coupled Autoregressive and Dynamical System
CCM	Cross-Correlation Method
CLSTM	Convolutional Long Short-Term Memory
CMD	Cloud Motion Displacement
CNN	Convolutional Neural Networks
CSL	Clear Sky Library
CSM	Clear Sky Model
DBN	Deep Belief Network
DCNN	Deep Convolutional Neural Networks
DHI	Diffuse Horizontal Irradiance
DL	Deep Learning
DNI	Direct Normal Irradiance
DNN	Deep Neural Network
ECMWF	European Centre for Medium-Range Weather Forecast
ELM	Extreme Learning Machine
ERA5	ECMWF Reanalysis v5
FTM	Fixed Threshold Method
GB	Gradient Boosting
GFS	Global Forecast System
GHI	Global Horizontal Irradiance

HCF	Haze Correction Factor
HRRR	High-Resolution Rapid Refresh
HSR	Hourly Solar Radiation
HYTA	Hybrid Thresholding Algorithm
ISR	Incident Solar Radiation
JMA	Japan Meteorological Agency
k-NN	k-Nearest Neighbors
LM	Levenberg-Marquardt
LST	Land Surface Temperature
LSTM	Long Short-Term Memory
MAE	Mean Absolute Error
MAPE	Mean Absolute Percentage Error
MBE	Mean Bias Error
MCE	Minimum Cross Entropy
MLP	Multi-Layer Perceptron
MM5	Mesoscale Model version 5
MOS	Model Output Statistics
MP	Megapixels
MSG	Meteosat Second Generation
MTF	Multi Transform Fusion
MVIRI	Meteosat Visible and InfraRed Imager
NAM	North Americam Mesoscale
NARMAX	Non-linear Autoregressive Models with Moving Average and Exogenous Input
NDFD	National Digital Forecast Database
NWP	Numerical Weather Prediction
PCA	Principal Component Analysis
PSM	Physical Solar Model Version 3
PSO	Particle Swarm Optimization
PV	Photovoltaic
RBM	Restricted Boltzmann Machine
RBR	Red-Blue Ratio
RF	Random Forest
RGB	Red Green Blue
RMSE	Root Mean Square Error
SAE	Stacker Automatic Encoder
SARIMA	Seasonal Autoregressive Moving Average
SDE	Standard Deviation
SOM	Self-Organizing Maps
SREF	Short Range Ensemble Forecast
SS	Skill Score
SVC	Support Vector Classifier
SVM	Support Vector Machines
SZA	Solar Zenith Angle
VARX	Vector Autoregressive with Exogenous Input
WC	Water Content
WNN	Wavelet Neural Network
WP	Water Path
WRF	Weather Research and Forecasting
WT	Wavelet Transform

Appendix A

Table A1. Summary of solar forecasting method.

Reference	Aim	Methods Utilized	Forecast Horizon	Data Period	Location	Input Variables	Comparison Methods	Performance Metrics	Results and Observations
[191]	Performance comparison of the ST, NWP, and MOS models, as well as the reference persistence model (PM)	ST MOS ANN MLPNN STNN ECMWF-MOSNN	24–72 h	January 2008–December 2011	Italy	GHI and air temperature	Naive persistence ECMWF-NWP	nMAE RMSE MAE MBE	The ST model and the NWP model give similar results. However, the sources of forecast errors between the ST and NWP models are identified. The MOS model gives the best performance, improving the forecast by approximately 29% with respect to the PM.
[5]	Non-parametric machine learning approach used for multi-site prediction of power generation	AR GBRT	6 h	April 2014–February 2015	Japan	Hourly average of power generation	Naive persistence K-fold Cross-validation Recursive AR Single-site Multi-site GRBT	RMSE nRMSE nMAE nMBE SS	A characteristics analysis demonstrates that variables related to lag observations are more important at the shorter forecast horizons. Over longer horizons, the importance of weather forecasts increases.
[6]	Simplified method for predicting hourly global solar radiation using extraterrestrial radiation	ANN K-means SVM LightGBM	1 h	2022	China	Solar irradiance	Naive persistence	RMSE MAE	Weather types were not the main factors that affected the prediction result of the model.
[8]	Hybrid solar irradiance forecasting framework using a K-means algorithm	TB K-means MLPNN	1–24 h	2004 and 2013	EEUU	Solar irradiance	Naive persistence	RMSE nRMSE Forecast Skill	This technique detects outliers and irregular patterns providing better characterization of the collected data.
[9]	Three types of forecast enhancements are proposed; in a uniform forecast when there is no ramp, ramp forecast magnitude enhancements, and ramp forecast threshold changes	NWP TSI KDE SVR eFAST	1 h	2006	EEUU	Solar energy index	Smart persistence	Correlation Coefficient RMSE nRMSE RMQE nRMQE MaxAE MAE MAPE MBE KSIPer OVERPer Std Skewness Kurtosis 95th Percentile Capacity	The distribution of forecast errors indicates that the relative forecast errors are smaller for a large geographic area.

Table A1. *Cont.*

Reference	Aim	Methods Utilized	Forecast Horizon	Data Period	Location	Input Variables	Comparison Methods	Performance Metrics	Results and Observations
[10]	Physics-based endogenous persistence method to forecast power output and ramps a few minutes earlier	Cloud speed persistence AR	180 s	6 July 2011–11 July 2012	EEUU	PV power outputs	Naive persistence Ramp persistence	rRMSE rMBE R skill	Excluding clear days and in terms of the mean square error percentage, the new method exceeded persistence by 16.2% at 20 s, 10.6% at 60 s, and 4.0% at 120 s forecast horizon.
[11]	Series of approaches based on whole-sky deep imaging learning architectures for very short-term solar PV generation forecasting	PM SPM SLNN SLNN-weather LSTM SIO SIH CNN-LSTM CNN-LSTM-H ConvLSTM ConvLSTM-H PredNet PredNet-H	Not applied	December 2018–February 2019	China	Sky images	Naive persistence SLNN SIH PredNet-H	RMSE nRMSE MAE MAPE	The proposed hybrid static imagery forecaster provides superior performance compared to benchmarking methods (i.e., those without sky images), with up to 8.3% improvement overall, and up to 32.8% improvement in the cases of ramp events.
[12]	Development of a model to forecast global horizontal irradiance (GHI) using only sky images without numerical measurements and additional feature engineering	CNN ANN LSTM	1 h	1981–1987	EEUU	GHI	ANN1 ANN2 GBM1 GBM2 GBM3 RF	RMSE MBE FSS	The model outperforms the benchmarking persistence of the cloud model and machine learning models with an nRMSE of 8.85% and an FSS of 25.14% in such a way that it shows superiority in various climatic conditions.
[13]	Development of classification forecasts based on pattern recognition for GHI forecasting	SVM	1 h	113 days of which 87 are summer	EEUU	Location Sky images Actual GHI measure-ments	Smart persistence	nMAE nRMSE	The results show that the developed short-term forecast framework outperforms the persistence benchmark by 16% in terms of the normalized Mean Absolute Error and by 25% in terms of the normalized mean square error.
[16]	Solar irradiance forecast for grid-connected PV plant	MLP	24 h	1 July 2008–23 May 2009 23 November 2009– 24 January 2010	Denmark	Irradiance G in the PV plane and air temperature	Cross validation	MBE RMSE r	98 to 99% for sunny days and 94 to 96% for cloudy days.

Table A1. *Cont.*

Reference	Aim	Methods Utilized	Forecast Horizon	Data Period	Location	Input Variables	Comparison Methods	Performance Metrics	Results and Observations
[17]	Solar irradiance forecast for grid-connected PV plant	Clear sky modeling with statistical smoothing techniques	Up to 36 h	2006	Not indicated	Power gained from 21 PV Temperature from NWP	Naive persistence	RMSE nRMSE	For horizons below 2 h, solar energy is the most important input, but for horizons the next day it is appropriate to use NWP as an input. RMSE 35% on persistence.
[18]	Assessment of the skill of the MM5 model	MM5	1–2 days	2012	Greece	Ground measurements of 11 radiometric stations	Not specified	MBE RMSE MAE	The seasonal analysis showed that the MM5 model tends to overestimate the GHI for all seasons of the year.
[19]	The methodology applied to introduce a large-scale, public, and solar irradiance dataset	ERA5 LR RF SVR	Every 30 min up to 24 h	2002–2019	Spain	Solar current every half hour	ERA5 LR RF SVR	RMSE MAE FS	The forecast error of a model can be reduced by adding variables from its neighboring stations.
[20]	PV power production forecasts under overcast skies	Clear sky model Clear sky index Kt Kalman filter	30 s–6 h	1 May 2011–30 April 2012	EEUU	PV power measurements every 15 min of 80 panels	Naive persistence	RMS MBE	Exceeds the persistence model for forecast horizons ranging from 30 min to 90 min. RMS = 0.062 MBE = 0.91
[22]	Calculation of incident radiation in clear skies on any inclined surface without the use of complicated meteorological instrumentation	MLP NARX	Next day	2006	Denmark	Historical PV power	Clear sky model	MAPE	The test results demonstrate that the forecasting model can be used to accurately forecast the daily power of the photovoltaic power system (MAPE = 16.47%).
[23]	Hybrid deep learning framework integrating convolutional neural network for pattern recognition with short-term memory network for global solar radiation (GSR) forecast every half hour	CLSTM hybrid model	1 day–1 week–2 weeks and 8 months every half hour	1 January 2006–31 August 2018	Australia	GSR	CNN LSTM DNN MLP Decision tree	MAE RMAE RMSE RRMSE MAPE APB KGE r	The hybrid model records superior results with more than 70% predictive errors below ± 10 Wm^{-2} and outperforms the reference model for GSR prediction every half hour of 1 day.
[24]	Short-term prediction of solar radiation, based on data collected in the near past	AR ARMA k-NN ELM SVR	Not specified	October 2005–October 2007	Italy	GHI database, weather station air temperature, and humidity	Naive persistence	Std Err(f)	The use of data collected from remote stations for short-term forecasts can be a useful alternative.

Table A1. *Cont.*

Reference	Aim	Methods Utilized	Forecast Horizon	Data Period	Location	Input Variables	Comparison Methods	Performance Metrics	Results and Observations
[25]	Application of an analog set method (AnEn) to generate probabilistic solar power forecasts (SPF)	AnEn QR Boca NN	3 days	60 days	Italy	PV powers and temperature of three sites	PeEn persistence set	CRPS MRE MAE	The different climatology in the three solar farms affects the performance of QR and AnEn particularly in terms of MAE (20–25%).
[26]	Analog set method for daily regional photovoltaic (PV) forecasting with resolution per hour	HDC EDAC NAM GFS SREF	NAM 84 h GFS 120 h SREF 87 h	7 January 2015–27 September 2016	EEUU	Historical temperature and irradiance data Astronomical data Current weather data	Naive persistence NWP model SVM model	nMAE NRMSE	The NRMSE has been reduced by 13.80% to 61.21% compared to the three baselines tested.
[29]	PV power forecasting model, considering the aerosol index data (AI) as an additional input parameter	BP-ANN	24 h	2 months	EEUU	Historical data for AI, PV power, temperature, humidity, and wind speed Current weather data	Error gradient descent algorithm	MAPE APPV	BP's neural network method has shown that the application of AI improves precision compared to conventional methods using ANN. MAPE = 7.65%.
[27]	Proposes a GHI, DNI, and DHI forecast model of solar irradiance using both AOD and data observed from a ground station	MLP SVR k-NN Decision tree regression	1 h	3 years	Saudi Arabia	KACARE AERONET CAMS	Smart persistence	RMSE FS	The MLP model is especially applicable for desert areas under clear sky conditions, where dust storms are frequent and AOD in the air is high. FS = 42%.
[28]	Aerosol-based solar irradiance forecasting for power applications system	Combination of aerosol forecasts with other measures	2–3 days	5 months	Germany, United King-dom, Italy, France, Spain, Netherlands	Aerosol concentration Albedo Ozone Water steam Cloud forecast (EURAD)	ECMWG MM5 Meteosat-7 data Ground measurements	RMSE rRMSE Bias rBias	The AFSOL system significantly improves global irradiance and especially direct irradiance forecasts relative to ECMWF forecasts (bias reduction from 226% to 111%; RMSE reduction from 31% to 19% for direct irradiance).
[33]	To accurately capture the effect of the cloud on irradiance, this article develops a real-time mapping model between the satellite image and solar irradiance	Image processing Deep CNN (VGG)	1–4 h	January 2017–November 2019	China	Satellite images GHI data Meteorological data	ANN MLP	RMSE MAE	The proposed hybrid method shows better precision and a smaller error range compared to other AI models. The proposed hybrid method could be applied to the forecast of regional or distributed photovoltaic energy.

Table A1. *Cont.*

Reference	Aim	Methods Utilized	Forecast Horizon	Data Period	Location	Input Variables	Comparison Methods	Performance Metrics	Results and Observations
[34]	GHI estimation using a combination of satellite and ANN images	ANN	30 min, 60 min, 90 min, 120 min.	1 January 2011–31 January 2012.	EEUU	Velocimetry Cloud indices using satellite images Irradiance data	Naive persistence	MBE RMSE	Combining stochastic learning, image processing and terrestrial telemetry provide benefits in the robustness and accuracy of prediction.
[35,71]	It combines ground measurements with exogenous inputs provided by satellites and PNT data. Using satellite data to improve prediction of solar radiation with Bayesian artificial neural networks	AR ARMA ANN. Bayesian ANN	1 h–6 h. 1 h–6 h	2005 2002 2003 2004 2005	Spain	Terrestrial data set Satellite-derived data: GHI and irradiation on top of the atmosphere ECMWF data set Terrestrial data and satellite data (Helioclim-3)	Smart persistence NN SAT ECMWF. Naive persistence Smart persistence CLI ANN	RMSE MAE Skill RMSE MAE Skill	The combination of exogenous satellite data and ECMWF data provides the best forecast results. The different results obtained in the southern and northern areas and depending on the set of quarterly seasonal data seem to be a consequence of cloud formation.
[36]	GHI's forecasting approach that relies on satellite imagery and ground measurements as inputs	Optical flow	1–2–3 h	110 days	EEUU	Satellite images Ground measurements	K-persistence model	MAE MBE RMSE	The method works reliably for optically thick clouds that are easily distinguished from the background, while problems persist with optically thin clouds (opaque). SS = 8–19%.
[37]	Analysis of ARMAX solar forecast models using ground measurements and satellite imagery	ARMAX	10 min 20 min 30 min 40 min 50 min 60 min 120 min 180 min 240 min	6 months	Argentina	Terrestrial data GHI Satellite albedo Local variability index	Naive persistence	MBD RMSD	All the models tested, whether or not they include exogenous variables, surpass the classic persistence procedure for the region.
[38]	Combination of whole sky images and irradiance measurements for irradiance forecasting and ramp event detection using the ramp detection index (RDI)	CSL FTM CCM	1–10 min	6 months	Uruguay	All-sky images GHI ground measurements	Regular persistence Smart persistence	MBD MAD RMSD RM RDI	The proposed method achieved a maximum yield of 11.4% in forecast horizons of 6 and 10 min in partially cloudy conditions.

Table A1. *Cont.*

Reference	Aim	Methods Utilized	Forecast Horizon	Data Period	Location	Input Variables	Comparison Methods	Performance Metrics	Results and Observations
[39]	Results of a very short-term horizontal irradiance forecasting (GHI) experiment based on images of the hemispheric sky are presented	RBR CSL Cloud and shadow mapping Gridding SVC Optical flow	Up to 25 min	2 months (April and May 2013)	Germany	Ground irradiance measure-ments Cloud heights using ceilometer All-sky images	Naive persistence	MBE RMSE FS ACC	The study shows that for distances of more than 1–2 km from the camera in cumulus cloud conditions, a single pyranometer outperforms.
[40]	System approach with four spatially distributed ASIs that manages to apply an individual 3D model of each detected cloud as a cloud object with different attributes	CSL RBR Voxel carving method Kalman filter	15 min	30 days	Spain	Ground irradiance measure-ments Alturas de nube mediante ceilómetro All-sky images	Validation of DNI maps by ground measurement	MAE rMAE	Spatially resolved DNI maps with a border length of 8 km.
[42]	Relationship between the appearance of the sky and future photovoltaic energy production using deep learning	MLP CNN LSTM	1 min	90 days	Japan	HDR hemispheric sky image data set and correspond-ing PV power	Naive persistence	MAE RMSE	MLP SS-RMSE = 7% CNN SS-RMSE = 12% LSTM SS-RMSE = 21%
[43,85]	Intelligent automatic cloud adaptive identification system (SACI) for projection of sky images and solar irradiance forecasting. Intelligent forecasting model for DNIs that combine sky image processing with ANN optimization schemes	CSL FTM MCE RBR ANN. GA ANN CVM RTM	1–5–10–15 min	5 March 2013–5 April 2013. 6 months	EEUU	80 images captured in Merced and 30 sky images captured in Folsom DNI data and sky images	Naive persistence. Naive persistence and deterministic model	MBE RMSE MBE RMSE	Forecast skills above 14%, 18%, and 19% above persistence forecast for 5, 10, and 15 min forecasts, respectively. The hybrid forecasting models proposed in this work achieve statistically robust forecasting abilities that exceed 20% on persistence for forecasts 5 and 10 min in advance, respectively.

Table A1. *Cont.*

Reference	Aim	Methods Utilized	Forecast Horizon	Data Period	Location	Input Variables	Comparison Methods	Performance Metrics	Results and Observations
[44]	Very short-term forecast of GHI and DNI solar irradiance using sky and optical flow cameras covering a variety of cloud conditions and more than ten different characteristics extracted from raw pixel data	Optical flow NN	30 min–2 h	24 months	Spain	All-sky images	Cross-validation 5 times	Bias	The applied method correctly classifies 95% of the clouds and with good forecasts, from low false positive rates of 0.08% to high overall accuracy rates of 96%.
[53]	A multivariate regression model that uses irradiance values measured from previous hours to improve predictions for the next hour, which can be used to refine daily strategies based on predictions for the next day	ECMWF TRNSYS SAM	1 day	1 July 2017–30 June 2018 1 July 2018–30 June 2019	Portugal	Ground irradiance data	Naive persistence	RMSE MSE MBE MAE r R2 SS	The proposed regression model significantly improves hourly predictions with a skill score of ≈0.84 (that is, an increase of ≈27.29% over the original hourly forecasts). The model shows a skill score of 70.78 (that is, an increase of ≈6% over the original forecasts).
[92]	Solar irradiance forecast from a ground-based sky imaging system evaluating its performance on thirty-one consecutive days of historical data collected during winter	CSL METAR CBH CCM	30 s–5 min	31 days of winter	EEUU	Sky images	Naive persistence	rRMSE rMBE rMAE FS	On average, frozen cloud advection forecasts were found to outperform image persistence forecasts for all forecast horizons during the analysis period. Forecast errors over various periods were attributed to inaccurate cloud base height (CBH).
[59]	A high-resolution cloud assimilation and numerical weather forecasting model for forecasting solar irradiance	WRF-CLDDA	36 h	3 days (06/19/11–06/21/11)	EEUU	Meteorological data	Naive persistence. NAM	rMBE rMAE rRMSE rSTDERR	WRF-CLDDA intraday forecasts had an rMBE of 0.4% compared to 17.8% for the NAM. Furthermore, rMAE was 21.3%, 4.1% lower than NAM. rSTDERR, was 2.4% higher than NAM, as a large part of the NAM error was attributed to systematic bias.
[60]	Short-term solar irradiance prediction with a hybrid ensemble model	ML DL	Every 1 min	2021	Austria	Satellite images	Ground measurements	R2 Score nMAE nRMSE	This method highlights the model's competency in capturing extremely high cloud variability during cloudy and heavily clouded sky conditions, resulting in a skill score improvement ranging from 10% to 30%.

Table A1. *Cont.*

Reference	Aim	Methods Utilized	Forecast Horizon	Data Period	Location	Input Variables	Comparison Methods	Performance Metrics	Results and Observations
[61]	Regional PV power estimation and forecasting using numerical and satellite weather forecast data	ANNsE Clustering	1–48 h	2014 and 2015	Italy	Satellite-derived irradiance data and numerical weather prediction (NWP)	Naive persistence Smart persistence	RMSE MAE SS	The model provided an intraday forecast (1 to 4 h) with an RMSE of 5–7% and a skill score with respect to intelligent persistence of -8% to 33.6%. The one and two-day ahead forecast achieved an RMSE of 7% and 7.5% and a skill score of 39.2% and 45.7%.
[62]	Examines two spatio-temporal approaches to the short-term forecast of global horizontal irradiance using satellite-derived grid irradiances as experimental support	STVAR CMV	1 h	2 years (2008, 2009)	Montserrat Island	Satellite-derived irradiance data from the SUNY database	Scaled persistence	RMSE rMAE rMBE Skill score	The performance of the model depends significantly on the orographic influence and the type of day (clear versus cloudy). It was found that the errors increased significantly with the orography of the location and the variability of the irradiance of the day
[63]	ANN accuracy is established along with satellite-derived Land Surface Temperature (LST) as a predictor to forecast solar radiation for the Queensland region	ANN	Monthly	2 years (2012–2014)	Australia	LST data	MLR ARIMA Cross-validation	r RMSE MAE WI RRMSE MAPE	The results showed that an ANN model outperformed the MLR and ARIMA models where analysis showed 39% cumulative errors in the smallest magnitude range, while MLR and ARIMA produced 15% and 25%.
[64]	Comparative study of LSTM neural networks to forecast daily global horizontal irradiance with satellite data	LSTM	1 day	2005–2014	Australia	Remote sensing data from the 2014 AMS Kaggle database	Smart persistence GBR FFNN	RMSE MAE SS	ML models understand atmospheric behavior even in cases of high variability. SS = 52.2%
[65]	GHI prediction using universally deployable extreme learning machines integrated with MODIS satellite predictors	ELM	6 h–1 day	2012–2015	Not indicated	Satellite data from the Moderate Resolution Imaging Spectroradiometer (MODIS)	RF M5 tree MARS	RMS	ELM versatility to generate forecasts on heterogeneous and remote spatial sites, surpassing all comparison models. RMS < 6% SS RMSE = 67.3%

Table A1. *Cont.*

Reference	Aim	Methods Utilized	Forecast Horizon	Data Period	Location	Input Variables	Comparison Methods	Performance Metrics	Results and Observations
[66,219]	Forecast method based on a phase correlation algorithm for estimating cloud movement derived from Meteosat-9 images. Two methods of extraction of motion vectors using correlation and optical flow methods	Phase correlation algorithm Heliosat-II method. Optical flow	4 horas 15 min–4 h	16 June 2012 at 1100 UTC 6 days daytime images Meteosat-10	France	Images of Meteosat-9 Images of Meteosat-10	Naive persistence	RMSE relative	The loss of precision compared to the existing method is still small, but real progress in time computing has been highlighted (25% reduction). Optical flow-based method outperforms all methods with satisfactory time calculation.
[112]	Hybrid prediction using satellite remote sensing data of surface solar irradiation coupled to a double exponential smoothing time series model	ARMA NAR-NN DES Interpolation method Kriging	1–2–3–4–5 days	2013–2015	Australia	EUMETSAT historical data	NWP-ANN ANN DCGSO-LASSO	RMSE MAPE r	The developed model provided very accurate forecasts, especially for the first four days.
[58]	Analysis of satellite imagery and an Exponential Smoothing State Space (ESSS) hybrid model along with artificial neural networks (ANN) for solar irradiance prediction	Image análisis EES ANN	Hourly	09/2010–07/2011	Japan	Cloud cover index Satellite images Irradiance dataset of the SERIS station	ARIMA LES SES RW	nRMSE nMBE R2	Compared to other popular statistical time series models such as ARIMA, LES, SES, and RW, the proposed model has superior forecasting accuracy.
[68]	Development and validation of a satellite-based GHI forecast for high latitudes (Finland)	CSM	Up to 4 h every 15 min	1 May 2016–31 August 2016	Finland	CS models data and satellite images	McClear SPECMAGIC Pvlib-python Solis	rMBE rRMSE	Good forecasting performance shows that satellite-based GHI forecasting methods are a viable option in PV forecasting also for high latitudes
[70]	Model proposal that can make short-term forecasts of solar irradiance at any general location without the need for measurements on the ground	DNN	Up to 6 h	1 January 2014–31 December 2017	Netherlands	Satellite measurements Weather forecasts Terrestrial data	6 ECMWF predicted values for 6 forecast hours CL irradiance Satellite images	rRMSE MBE	The proposed model is equal to or better than the local models. Savings in operating costs of installing local sensors and collecting ground data. rRMSE general = 31.31% rRMSE local = 31.01%

Table A1. *Cont.*

Reference	Aim	Methods Utilized	Forecast Horizon	Data Period	Location	Input Variables	Comparison Methods	Performance Metrics	Results and Observations
[75]	Method based on advanced machine learning algorithms for the selection and prediction of variables	NN RVS	5–60 min	1 January 2013–31 December 2014	Italy	Previous PV data and previous weather data	Baseline B1 Baseline B2	MAE MRE	PV power production for very short-term forecast horizons of 5 to 60 min can be accurately predicted using only past PV data, without weather information.
[78,89,90]	Solar immediate prediction system based on shadow cameras for short-term forecasts and generation of DNI maps The validation of GHI and DNI maps projected from an example system consisting of 4 cameras for the entire sky WobaS-4cam is presented The validation of GHI and DNI maps projected from an example system consisting of 4 cameras for the entire sky WobaS-4cam is presented	KCF CSR-DCF. CSL. CSL	1–2 min 0–15 min 0–15 min	8 September 2015–14 January 2016. 30 days between September 2015 and October 2016. 30 days between September 2015 and October 2016	Spain	Soil images and meteoro-logical data Sky images Ground irradiance measure-ments Terrestrial images from shadow cameras Sky images Ground irradiance measure-ments Terrestrial images from shadow cameras	Wobas-2cam Ground measurements Terrestrial images. Ground measurements Terrestrial images	rRMSD rMAD rBias TDI. MAE rMAE bias rbias RMSE rRMSE std rstd MAE rMAE bias rbias RMSE rRMSE std rstd	Compared to a whole sky imaging system, better results are achieved for 1 and 2 min forecasts. Spatial aggregations reduce RMSE (GHI) values from 21.4% to 13.0%. Time averaging reduces RMSE (GHI) deviations from 25.3% (mean delivery time 7.5 min, time averaging 1 min) to 19.0% (mean delivery time 7.5 min, time averaging 15 min). Las agregaciones espaciales reducen los valores de RMSE (GHI) del 21.4% al 13.0%. El promedio temporal reduce las desviaciones de RMSE (GHI) del 25.3% (tiempo de entrega medio 7.5 min, promedio temporal de 1 min) al 19.0% (tiempo de entrega medio 7.5 min, promedio temporal de 15 min).
[91]	Short-term solar forecasting system using low-cost ground-based sky imaging cameras	NN Optical flow	0–20 min	2 years	Australia	Sky images	Smart persistence	Accuracy Metrics	This model can be easily adapted for conservative or aggressive operation of a solar power system with a backup generator.
[94]	Estimation of cloud movement and stability for intra-hourly solar forecasting	VOF CCM	5–10–15 min	1 month (November 2012)	EEUU	Sky images	Smart persistence CCM	Cloud Index FS	The VOF forecast with a fixed smoothness parameter was found to be superior to the image persistence forecast for all forecast horizons for almost every day and exceeds the CCM forecast with an average error reduction of 39%, 21%, 19%, and 19% for 0, 5, 10, and 15 min forecasts, respectively.

Table A1. *Cont.*

Reference	Aim	Methods Utilized	Forecast Horizon	Data Period	Location	Input Variables	Comparison Methods	Performance Metrics	Results and Observations
[102]	3D cloud detection and tracking system for solar forecasting using multiple sky imagers	Image processing SVM Stereographic calculations for cloud height Clustering Multi-layer aggregation	1–15 min	13 May 2013–3 June 2013	EEUU	Sky images GHI measurements	Smart persistence	STI MAE RMSE	Compared to the persistent model, the system achieves at least a 26% improvement for all irradiance forecasts between one and fifteen minutes, as well as robustly tracking layers.
[103–105]	Hybrid solar irradiance prediction method by merging the Kalman filter and a regression predictor. Prediction of slowdown events through improved cloud detection and tracking A mechanism for predicting dimming and deceleration events based on tracking and grouping information is proposed	Filtro de Kalman Regresor de predicción. RBR SVM Random forest Bayesian classifier Kalman filter Prediction regressor Clustering algorithm Markov SVM	10–20 min. 10–15 min. 5–10–15–20 min	January 2014–September 2014. January 2014 May 2014 Not specified	EEUU, Taiwan, Taiwan	Ground irradiance measurements Sky images Ground irradiance measurements Sky images Ground irradiance measurements Sky images	Naive persistence 3 NN fusion alternatives. ANN HYTA Compared with its previous models	RMSE MAE RMSE MAE RMSE MAE	Experiments have shown that the time-varying system matrix design is useful in improving the prediction result of the Kalman filter and the proposed hybrid predictor outperforms all other methods being compared. Deceleration events are forecast according to the predicted position of the sun and the movement of clouds. The method could help grid operators make better use and management of solar energy resources.

Table A2. Summary of solar prediction method.

Reference	Aim	Methods Used	Forecast Horizon	Data Period	Input Variables	Comparison Methods	Performance Metrics	Results and Observations
[108]	2D cloud map generation from sky cover	CSL RBR CCM	30 s–5 min	14 September 2009–10 March 2010	Sky images	Cloud persistence	TSI	Cloud shadows in outer regions are now correctly cast 70% of the time.
[111]	Deep learning-based approach to next-day solar PV forecast task	DL	24 h	1 January 2015–31 December 2016	PV power	PSF NN	RMS MAE	The proposed deep learning approach is particularly suitable for solar big data, given its linear time increment behavior, contrary to PSF and NN which show an exponential time increment.

Table A2. *Cont.*

Reference	Aim	Methods Used	Forecast Horizon	Data Period	Input Variables	Comparison Methods	Performance Metrics	Results and Observations
[112]	Methodology to forecast the energy production of photovoltaic solar energy by using ARMA	ARMA	1 h	1 year	PV power	Naive persistence Smart persistence	MAE RMSE	The proposed model works better than an intelligent persistence model and is suitable for use in stochastic or robust optimization models for the operation and planning of the electrical system.
[113]	Solar energy forecasting algorithm based on the vector autoregression framework, combining distributed time series information collected by the smart grid infrastructure	VAR VARX AR Gradient boosting	1–6 h	Not specified	PV power	Not specified	RMSE	Real data results from a test pilot show that information from distributed PV generation, when combined into a common forecasting framework, can improve point forecasting ability, compared to a univariate model between 8% and 10%, with 12% on average.
[114]	ARMAX model to forecast the energy production of a photovoltaic system connected to the grid	ARMAX	1 day	1 January 2011–30 June 2012	Historical PV power	ARIMA NN	RMSE MAD MAPE	The ARMAX model is shown to greatly improve the output power forecasting accuracy over the ARIMA model.
[115]	This study aims to develop a SARIMA model to predict daily and monthly solar radiation in Seoul, South Korea, based on hourly solar radiation data	SARIMA ACF PACF	Daily and monthly	37 years (1981–2017)	Solar irradiance	SARIMA	RMSE	The results indicate that (1,1,2) the ARIMA model can be used to represent daily solar radiation, while the SARIMA (4,1,1) of 12 lags for both auto-regressive and moving average parts can be used to represent monthly solar radiation.
[116]	SARIMA model for multi-step forecasting (20 min resolution) of photovoltaic solar generation	SARIMA ACF	Every 20 min	April 2017	PV power	Naive persistence	Modified MAPE	Although model performance is considered satisfactory on sunny days (clear skies), it can degrade on cloudy days when solar PV generation is more intermittent. Therefore, the model may not be suitable for very short-term forecasts in months that have cloudy or rainy days.
[124]	A model based on Mycielski is proposed that considers the hourly recorded solar radiation data as a matrix and, from the last record value, tries to find the most similar sub-matrix pattern in history	Mycielski Markov	1 h	4 and 2 years for each of the two different sites	Solar irradiance	Actual irradiance data	RMSE R^2 MABE	Test results between 2-year and 4-year solar radiation data show that using more historical data, for example, more years like 6 or 8, will increase the accuracy of both models.

Table A2. *Cont.*

Reference	Aim	Methods Used	Forecast Horizon	Data Period	Input Variables	Comparison Methods	Performance Metrics	Results and Observations
[126]	Solar power forecasting with random forest based on ranking optimization	PCA K means clustering Random Forest	Hourly	1 April 2012–29 June 2012	GEFCom2014 energy forecast data	SVM ANN Decision tree Gaussian regression model	MAE RMSE	By establishing comparative experiments, the recommended model is found to have higher prediction accuracy and robustness.
[129]	CARDS solar forecast, developed at the University of South Australia, for forecasting solar radiation series at three sites in Guadeloupe in the Caribbean	CARDS ARCH	4 h	Each minute	Solar irradiance	Cross-correlation	MAPE MBE nRMSE	The final noise terms, obtained after the Fourier series models, the CARDS modeling, and the cross-correlative models, exhibit conditional volatility, which is also subject to cross-correlative effects.
[130]	Forecast of solar radiation on an hourly time scale using a CARDS model	CARDS	1 h	1 year (2000)	GHI	DRWNN TDNN-ARMA Kaplani's model	MAPE MBE nRMSE KSI	The results of the error analyses show that the CARDS model has reduced the forecast error of the combination model by 33.4% for ASM.
[131]	Comparison of models with delivery times ranging between 1 and 6 h and that use only endogenous inputs to generate forecasts	ARMA CARDS NN LMQR WQR QRNN GARCHrls SB QRF GBDT	1–6 h	2 years	GHI Clear sky index	Smart persistence	RMSE MAE MBE FS	The combination of the models leads to a comparison of 20 probabilistic forecasts. LMQR, WQR, and GBDT are the most efficient models to generate probabilistic forecasts without the use of exogenous variables.
[132]	Approach to predicting solar radiation series one hour in advance using various multiscale decomposition techniques of clear sky index Kc data	EMD EEMD Wavelet de-composition AR NN	5 min–6 h	January 2012–December 2013	Solar irradiance measurements	Naive persistence	rRMSE rMBE rMAE s	From the multi-scale decomposition, the accuracy of the solar forecast is significantly improved. For example, in terms of RMSE error, the forecast obtained with the classic NN model is around 25.86%, this error decreases to 16.91% with the EMD-Hybrid model, to 14.06% with the EEMD model hybrid and at 7.86% with the WD-hybrid model.

Table A2. *Cont.*

Reference	Aim	Methods Used	Forecast Horizon	Data Period	Input Variables	Comparison Methods	Performance Metrics	Results and Observations
[133]	Method for multi-month forecast of monthly mean daily global solar radiation time series and data-driven large-scale solar radiation forecast	ARMA ARIMA	1–2–3 months	November 2018–March 2019	Data collected from Meteonorm 8 software	Naive persistence	MBE RMSE MAPE T_s Sd	ARIMA (0, 2,1) is more suitable for forecasting the monthly mean daily global solar radiation for the city of Tetouan and may be so for other locations with similar climatic conditions.
[134]	A data-driven framework is proposed for forecasting solar irradiance based on the fusion of spatial and temporal information	BRT ANN SVM LASSO	30–60–90–120 min	2014–2015	GHI	Smart persistence AR ARX	nRMSE R^2 S	The computational results of the multi-step ahead prediction demonstrate that the BRT model offers the best performance with the lowest normalized Root Mean Square Error of 18.4%, 24.3%, 27.9%, and 30.6% for prediction horizons of 30, 60, 90, and 120 -min, respectively.
[136]	Short-term solar irradiance forecasting is conducted using WNN trained with GD and LM training, and SNN trained with LM training	WNN with LM and GD training	1–2–4–6 h	3 years (2007–2009)	Solar irradiance	SNN with training GD	MAPE RMSE	The proposed model has better generalizability and more precision than the conventional sigmoid neural network (SNN).
[137]	Prediction of solar radiation per hour using a wavelet neural network and using the average daily solar radiation	WNN	Hourly	5 years	Angle of the sun at sunset and sunrise Daily solar radiation	HSR data	MAPE RMSE	The 96% of R^2, demonstrates that the model can be easily implemented and can increase the precision of the estimate.
[138]	Mixed wave neural network (WNN) in for the forecast of solar irradiance in the short term, with initial application in the tropical zone	WNN	15 min–1 h	1 year (2014)	Clear sky index values Kc	Naive persistence ETS ARIMA ANN	MBE nRMSE	The key advantage of using WT methods is the high signal compression capacity, which makes them suitable for modeling non-stationary environmental parameters with high information content, such as short time scale solar irradiance. Optimal WNN architecture varies by season.
[139]	A solar irradiance forecasting method for remote microgrids based on the Markov switching model is presented	MSM Fourier basis expansion	1 day	1998–2013	Historical irradiance data	Error between years	MAPE RMSE	The study resulted in a Mean Absolute Percentage Error of 31.8% over five years, from 2001 to 2005, with higher errors during the summer months.

Table A2. *Cont.*

Reference	Aim	Methods Used	Forecast Horizon	Data Period	Input Variables	Comparison Methods	Performance Metrics	Results and Observations
[141]	Hybrid deep learning framework integrating convolutional neural network for pattern recognition with short-term memory network for global solar radiation (GSR) forecast every half hour	CLSTM hybrid model	1 day–1 week–2 weeks and 8 months every half hour	1 January 2006–31 August 2018	GSR	CNN LSTM DNN MLP Decision tree	MAE RMAE RMSE RRMSE MAPE APB KGE r	The hybrid model registers superior results with more than 70% of predictive errors below ± 10 Wm^{-2} and exceeds the reference model for the prediction of GSR every half hour of 1 day.
[146]	Deep learning for solar power forecasting using an approach using an autoencoder and LSTM neural networks	Deep Belief Networks Autoencoder LSTM	24–48 h	990 days	PV power from GermanSolar-Farm	P-PVFM	RMSE MAE AbsDev Bias Correlation	The best-performing model is the Auto-LSTM with an RMSE of 0.0713, closely followed by the DBN with an RMSE of 0.0714. This shows the feature extraction capabilities of these models, allowing for a good solar power forecast. Both models without this capability, the MLP and the LSTM without AE, perform worse.
[147]	Forecast approach for irradiance time series that combines mutual information measurements and an extreme learning machine (ELM). The method is known as Minimum Redundancy—Maximum Relevance (MRMR)	IFS-based MRMR ELM	15 min–1 h-24 h	Measurements at 20 sites every minute for 2 years	Solar irradiance data	*Long window* *Short window* PCA MRMR	R^2 MAPE nMSE RMSE FS	The performance criteria indicate that the MRMR method clearly outperforms the other dimensionality reduction scenarios in most cases. Compared to other machine learning techniques, ELM has the advantage of achieving good performance in terms of accuracy in extremely fast computational time.
[148]	Hybrid mapping based on applied deep learning for solar PV forecasting	CNN LSTM K-means clustering Convolutional Autoencoder	Not specified	1 July 2017–30 June 2018	25,000 all-sky images	RMSE MAE CORR	CNN LSTM ANN	The proposed hybrid mapping model shows better precision, and a smaller error range compared to other deep learning methods.
[149]	Short-term solar power forecasting with deep learning: exploration of the optimal input and output configuration using hybrid data, temporal history, and strong regularization	CNN	15 min	1 March 2017–1 March 2028	Sky images PV power	Smart persistence AR	RMSE FS	It achieves a forecast ability of 15.7% on the overall test suite and 16.3% on the most demanding cloudy days, relative to the smart persistence model. Careful downsampling can reduce training time by up to 83% without affecting accuracy.

Table A2. *Cont.*

Reference	Aim	Methods Used	Forecast Horizon	Data Period	Input Variables	Comparison Methods	Performance Metrics	Results and Observations
[151]	A strategy that uses artificial intelligence (AI) to forecast irradiance directly from an extracted sub-image that surrounds the sun	Optical flow Ray tracing CNN GLM MLP RFR GBT	15 min	October 2015–May 2016 (147 días)	Sky images	MLP Deep Learning RFR GBT	MAE MAPE nRMSE R^2	Several different AI models are compared, including deep learning and Gradient Boosted Trees. (MLP R^2 = 0.71, RF R^2 = 0.76, DL R^2 = 0.871, GBT R^2 = 0.875).
[156]	High-resolution real-time NWP results based on the weather forecasting and research (WRF) model study the ability of the model to provide daytime GHI and clear sky index predictions	MOS	2–5 days	1 August 2015–31 December 2016	GHI DRI forecast data	WRF	MBE rMBE MAE rMAE RMSE rRMSE r	The importance of developing a seasonal and site-specific climate-dependent model output statistics (MOS) approach is shown to improve forecast accuracy, eliminating bias and reducing the overall relative mean square error (rRMSE) of GHI. as much as 6%, compared to the uncorrected model output.
[159]	The method is based on the advection and diffusion of estimates of the Meteosat Second Generation (MSG) cloud index using the numerical weather prediction (NWP) model of meteorological research and forecasting (WRF)	WRF	Up to 6 h with 15 min resolution	25 days	GHI and DNI of three sites Cloud height by ceilometer Sky images Satellite images	Smart persistence OpenPIV CMV WRF-Solar	RMSE Bias Skill	The results showed that the model is capable of providing improved forecasts in areas with low topographic complexity, where the advection of clouds by the dynamics of the atmospheric mesoscale is not disturbed by the characteristics of the mountains (the model t outperforms the OpenPIV method (∼5% rRMSE), smart persistence (∼10–20% from 1 to 5 h of waiting time) and WRF-Solar (∼10–30% until the fourth forecast hour).
[160]	Proposes a framework of stochastic differential equations to model the uncertainty associated with the prediction of the solar irradiance point	SDE Kalman filter Lamperti transform	1 h–24 h	01/01/09–31/12/11	NWP irradiance predictions Solar irradiance measurements	Naive persistence	Training and testing	The combination of the extended Kalman filter and the Lamperti transform offers a flexible framework for estimating SDE with a relatively large number of data points. In addition, the in-sample and out-of-sample results indicate that the linearization introduced by the filter works satisfactorily.
[161]	The purpose of this work is to establish a methodology to produce solar irradiance forecasts using WRF combined with a post-processing method	WRF ANDS ANNS BSNR	1 h	2009–2011	Solar irradiance	WRF ANN	RMSE ME MSE	The study showed that the precisions derived from the ANN model had lower deviations in bias, MSE and RMSE increased the correlation coefficients in the dry and rainy seasons. In both seasons, the ANN model provided forecasts with a significant reduction in deviations compared to the WRF model.

Table A2. *Cont.*

Reference	Aim	Methods Used	Forecast Horizon	Data Period	Input Variables	Comparison Methods	Performance Metrics	Results and Observations
[162]	State-of-the-art implementations of climate research and forecasting are combined with multivariate statistical learning techniques	RTM WRF GFS MOS UR	De 5 a 6 h	From 2016 with data from 9 am to 5 pm	GHI of 25 different SERIS stations	Naive persistence	RMSE MAE MBE	It is concluded that WRF Solar is a significant improvement over the WRF standard with RRTMG. It is shown that, without statistical processing, WRF is a significant improvement over the global model. The multivariate model output statistics routine improves forecasts on all our models.
[163]	An evaluation of the solar irradiance forecasts of the Global Forecast System is provided	ANN ARN BSRN NWP BRL	1 day	1 January 2015–31 December 2016	Data from various weather stations in China	Naive persistence	MAE RMSE MBE	Statistical indicators show that GHI and DNI forecasts are generally overestimated by GFS, seeing that DNI is more complicated to predict than GHI.
[164]	A corrective algorithm is proposed to improve the accuracy of the global horizontal irradiation (GHI) forecasts obtained from the numerical climate prediction model	ANN SVM RRTM	4–24 h	May 2015–November 2016 January 2015–November 2016	Meteorological variables	Smart persistence ECMWF ARIMA FFT	MBE MAE RMSE U95 R^2 TS GPI FS	The GHI forecasts obtained from the IFS were shown to be more accurate for clear sky conditions, slightly underestimating the GHI value with MBE ranging from −6.46 to −9.14 w/m^2.
[165]	A hybrid forecasting model is proposed that combines Wavelet transform, swarm particle optimization and SVM for short-term generation power forecasting	NWP COSMO WRF RAMS MM5 PSO SVM WT	3–24 h	May 2014–April 2015	Meteorological variables	BPNN HGNN HPNN SVM HGS HPS HHPS	MAPE RMSE nMAE SSE SDE	The daily MAPE and NMAE have average values of 4.22% and 0.4%, respectively, surpassing other seven prediction strategies, while the average calculation time is less than 15 s. Therefore, the effectiveness for the prediction of photovoltaic solar energy in the short term is verified.
[168]	Preprocessing of WRF initial conditions for coastal stratocumulus prediction	WEMPP CLDDA WRF	5–10–30 min	1 month	NAM and RAP data set	Comparison with ground measurements Naive persistence	MBE MAE	It is shown that the combination of both preprocessors provided improvement in the prediction of the spatial coverage, the thickness, and the useful life of Sc in the coastal regions where stratocumulus of the marine layer is observed more frequently, but the cloud cover over the ocean by all the preprocessors.

Table A2. *Cont.*

Reference	Aim	Methods Used	Forecast Horizon	Data Period	Input Variables	Comparison Methods	Performance Metrics	Results and Observations
[169]	A solar energy prediction model based on several satellite images and a supporting machine learning (SVM) scheme is proposed	SVM AMV ANN ARMA ARIMA NAR	Up to 1 h	April 2011–September 2015	Satellite images	Smart persistence GHI	RMSE MRE R^2	Throughout the experiments, the proposed SVM-based prediction model shows the highest prediction precision, compared to other prediction models, such as conventional time series and ANN models.
[170]	Satellite-based model fusion technique designed for short-term solar irradiance ramp forecasting	NWP CLAVR-x CIRACast SASRAB	Up to 3 h	January 2014–December 2016	Images taken from satellite	SURFRAD GHI	nMAE MAPE RMSE	Typical errors range from 8.5% to 17.2%, depending on the complexity of the cloud regimes, and an operational demonstration exceeded the forecast based on persistence of global horizontal irradiance (GHI) under all conditions by ~10 W/m^2.
[171]	Surface solar radiation forecast algorithm using enhanced visible and infrared image cloud physical properties (SEVIRI)	HARMONIE KNMI SICCS CMVS	Up to 4 h	September 2016–April 2017	Satellite images	SEVIRI	RMSE	The quality of the prediction depends on the weather conditions. CMVs using 5 images give better results for the radar advection algorithm.
[173]	Estimation of solar irradiance using MSG images comparing each radiation component with the average value of the previous 15 min	ESRA Heliosat-2	Hourly	2010–2014	Satellite data	Average radiation value of the previous 15 min	RMSE nRMSE MBE nMBE R	The nRMSE value for global estimates is approximately 7%, for beam estimates it is approximately 18%, and for diffuse estimates it is 16%. Under clear skies, the evaluation indicators present the best results.
[175]	Identification of relationships between the accuracy of an intraday surface solar irradiance forecasting method and meteorological variables that can be easily observed or predicted	ARPEGE CMV	Up to 6 h	July 2017–June 2020	Satellite images	FS	RMSE MBE MAE R	The results can help solar users anticipate the forecast start time up to several days in advance. SS positive forecast is achieved compared to persistence (up to 15%) and numerical weather predictions (between 20% and 40%).
[209]	Solar irradiance forecasting method based on real-time surface irradiance mapping model, which is beneficial to achieve higher accuracy in solar energy forecast	RGB model Distortion correction CDV FPC BPNN SVM	Every minute (real time)	De 7.00 a 17.00 del 2 May 2017, 26 August 2016 y 8 June 2018	Sky images Meteorological variables	ARIMA BPNN with meteorological variables as input	MAPE RMSE MBE	The average measurements of the proposed method using MAPE, RMSE, and MBE are 22.66%, 92.72, −1.26% for block clouds; 20.44%, 132.15, −1.06% for thin clouds and 18.82%, 120.78, −0.98% for thick clouds, thus offering a much higher forecast accuracy than other points of reference.

Table A2. *Cont.*

Reference	Aim	Methods Used	Forecast Horizon	Data Period	Input Variables	Comparison Methods	Performance Metrics	Results and Observations
[212]	Predicting cloud movement with an image registration approach	Thirions Demons Fischer	20 s	In real time	Image acquisition	Chow method	Not Specified	The proposed method improves the block combination strategy by 19%.
[215]	Method to track and predict cloud movement with ground-based sky images	Lucas-Kanade	30–40 s	In real time	640 × 480 pixels partial sky images	With himself	UCSD	The presented method has the potential to track clouds traveling in different directions and at different speeds.
[220]	Various sky image processing techniques relevant to solar prediction are described, including velocity field calculations, spatial transformation of images, and cloud classification	MPIV K-means algorithm	3–15 min	Every minute for 4 highly variable days	Sky images	Naive persistence	RMSE	RMSE errors demonstrate that sky imagers are useful for forecast horizons 3 to 15 min in advance. Compared to a persistent model, it appears that the most significant forecast accuracies are for 5 min ahead.

References

1. Angelis-Dimakis, A.; Biberacher, M.; Dominguez, J.; Fiorese, G.; Gadocha, S.; Gnansounou, E.; Guariso, G.; Kartalidis, A.; Panichelli, L.; Pinedo, I.; et al. Methods and tools to evaluate the availability of renewable energy sources. *Renew. Sustain. Energy Rev.* **2011**, *15*, 1182–1200. [CrossRef]
2. Boyle, C.F.; Haas, J.; Kern, J.D. Development of an irradiance-based weather derivative to hedge cloud risk for solar energy systems. *Renew. Energy* **2021**, *164*, 1230–1243. [CrossRef]
3. Cornaro, C.; Pierro, M.; Bucci, F. Master optimization process based on neural networks ensemble for 24-h solar irradiance forecast. *Sol. Energy* **2015**, *111*, 297–312. [CrossRef]
4. Lorenz, E.; Remund, J.; Müller, S.C.; Traunmüller, W.; Steinmaurer, G.; Pozo, D.; Ruiz-Arias, J.A.; Lara Fanego, V.; Ramirez, L.; Romeo, M.G.; et al. Benchmarking of Different Approaches to Forecast Solar Irradiance. In Proceedings of the 24th European Photovoltaic Solar Energy Conference, Hamburg, Germany, 21–25 September 2009. [CrossRef]
5. Persson, C.; Bacher, P.; Shiga, T.; Madsen, H. Multi-site solar power forecasting using gradient boosted regression trees. *Sol. Energy* **2017**, *150*, 423–436. [CrossRef]
6. Yang, X.; Ji, Y.; Wang, X.; Niu, M.; Long, S.; Xie, J.; Sun, Y. Simplified Method for Predicting Hourly Global Solar Radiation Using Extraterrestrial Radiation and Limited Weather Forecast Parameters. *Energies* **2023**, *16*, 3215. [CrossRef]
7. Antonanzas, J.; Urraca, R.; Pernía-Espinoza, A.; Aldama, A.; Fernández-Jiménez, L.A.; Martínez-de-Pisón, F.J. *Single and Blended Models for Day-Ahead Photovoltaic Power Forecasting de HAIS 2017: Hybrid Artificial Intelligent Systems*; Springer: Cham, Switzerland, 2017. [CrossRef]
8. Pedro, H.T.C.; Coimbra, C.F.M. Assessment of forecasting techniques for solar power production with no exogenous inputs. *Sol. Energy* **2012**, *86*, 2017–2028. [CrossRef]
9. Zhang, J.; Florita, A.; Hodge, B.-M.; Lu, S.; Hamann, H.F.; Banunarayanan, V.; Brockway, A.M. A suite of metrics for assessing the performance of solar power forecasting. *Sol. Energy* **2015**, *111*, 157–175. [CrossRef]
10. Lipperheide, M.; Bosch, J.; Kleissl, J. Embedded nowcasting method using cloud speed persistence for a photovoltaic power plant. *Sol. Energy* **2015**, *112*, 232–238. [CrossRef]
11. Kong, W.; Jia, Y.; Dong, Z.Y.; Meng, K.; Chai, S. Hybrid approaches based on deep whole-sky-image learning to photovoltaic generation forecasting. *Appl. Energy* **2020**, *280*, 115875. [CrossRef]
12. Feng, C.; Zhang, J. SolarNet: A sky image-based deep convolutional neural network for intra-hour solar forecasting. *Sol. Energy* **2020**, *204*, 71–78. [CrossRef]
13. Feng, C.; Cui, M.; Lee, M.; Zhang, J.; Hodge, B.-M.; Lu, S.; Hamann, H.F. Short-term global horizontal irradiance forecasting based on sky imaging and pattern recognition. In Proceedings of the 2017 IEEE Power & Energy Society General Meeting, Chicago, IL, USA, 16–20 July 2017. [CrossRef]
14. Rodríguez-Benítez, F.J.; López-Cuesta, M.; Arbizu-Barrena, C.; Fernández-León, M.M.; Pamos-Ureña, M.; Tovar-Pescador, J.; Santos-Alamillos, F.J.; Pozo-Vázquez, D. Assessment of new solar radiation nowcasting methods based on sky-camera and satellite imagery. *Appl. Energy* **2021**, *292*, 116838. [CrossRef]
15. Ma, Y.; Lv, Q.; Zhang, R.; Zhang, Y.; Zhu, H.; Yin, W. Short-term photovoltaic power forecasting method based on irradiance correction and error forecasting. *Energy Rep.* **2021**, *7*, 5495–5509. [CrossRef]
16. Mellit, A.; Pavan, A.M. A 24-h forecast of solar irradiance using artificial neural network: Application for performance prediction of a grid-connected PV plant at Trieste, Italy. *Sol. Energy* **2010**, *84*, 807–821. [CrossRef]
17. Bacher, P.; Madsen, H.; Nielsen, H.A. Online short-term solar power forecasting. *Sol. Energy* **2009**, *83*, 1772–1783. [CrossRef]
18. Kosmopoulos, P.; Kazadzis, S.; Lagouvardos, K.; Kotroni, V.; Bais, A. Solar energy prediction and verification using operational model forecasts and ground-based solar measurements. *Energy* **2015**, *93*, 1918–1930. [CrossRef]
19. Cesar, L.B.; Callejo, M.M.; Cira, C.-I.; Alcarria, R. CyL-GHI: Global Horizontal Irradiance Dataset Containing 18 Years of Refined Data at 30-Min Granularity from 37 Stations Located in Castile and León (Spain). *Data* **2023**, *8*, 65. [CrossRef]
20. Lonij, V.P.; Brooks, A.E.; Cronin, A.D.; Leuthold, M.; Koch, K. Intra-hour forecasts of solar power production using measurements from a network of irradiance sensors. *Sol. Energy* **2013**, *97*, 58–66. [CrossRef]
21. Jananni, K.; Swetha, S.; Vaitheeswari, V.B. Performance Analysis of Automated Solar Panel Tracking System. In Proceedings of the 2022 2nd International Conference on Advance Computing and Innovative Technologies in Engineering (ICACITE), Greater Noida, India, 28–29 April 2022; pp. 1968–1971. [CrossRef]
22. Tao, C.; Shanxu, D.; Changsong, C. Forecasting power output for grid-connected photovoltaic power system without using solar radiation measurement. In Proceedings of the 2nd IEEE International Symposium on Power Electronics for Distributed Generation Systems (PEDG), Hefei, China, 16–18 June 2010. [CrossRef]
23. Ghimire, S.; Deo, R.C.; Downs, N.J.; Raj, N. Global solar radiation prediction by ANN integrated with European Centre for medium range weather forecast fields in solar rich cities of Queensland Australia. *J. Clean. Prod.* **2019**, *216*, 288–310. [CrossRef]
24. Lazzaroni, M.; Ferrari, S.; Piuri, V.; Salman, A.; Cristaldi, L.; Faifer, M. Models for solar radiation prediction based on different measurement sites. *Measurement* **2015**, *63*, 346–363. [CrossRef]
25. Alessandrini, S.; Monache, L.D.; Sperati, S.; Cervone, G. An analog ensemble for short-term probabilistic solar power forecast. *Appl. Energy* **2015**, *157*, 95–110. [CrossRef]
26. Zhang, X.; Li, Y.; Lu, S.; Hamann, H.F.; Hodge, B.-M.S.; Lehman, B. A Solar Time Based Analog Ensemble Method for Regional Solar Power Forecasting. *IEEE Trans. Sustain. Energy* **2018**, *10*, 268–279. [CrossRef]

27. Alfadda, A.; Rahman, S.; Pipattanasomporn, M. Solar irradiance forecast using aerosols measurements: A data driven approach. *Sol. Energy* **2018**, *170*, 924–939. [CrossRef]
28. Breitkreuz, H.; Schroedter-Homscheidt, M.; Holzer-Popp, T.; Dech, S. Short-Range Direct and Diffuse Irradiance Forecasts for Solar Energy Applications Based on Aerosol Chemical Transport and Numerical Weather Modeling. *J. Appl. Meteorol. Clim.* **2009**, *48*, 1766–1779. [CrossRef]
29. Liu, J.; Fang, W.; Zhang, X.; Yang, C. An Improved Photovoltaic Power Forecasting Model With the Assistance of Aerosol Index Data. *IEEE Trans. Sustain. Energy* **2015**, *6*, 434–442. [CrossRef]
30. Kelvin, T.H.C.; Brindley, H.; Ekins-Daukes, N.; Escobar, R. Developing automated methods to estimate spectrally resolved direct normal irradiance for solar energy applications. *Renew. Energy* **2020**, *173*, 1070–1086. [CrossRef]
31. Merchant, C.; Meggers, F. Resolving the Full Radiant Spectrum: Solving the Shortwave Imaging Problem for Enhanced Radiant Energy Analysis. In Proceedings of the 2022 IEEE International Workshop on Metrology for Living Environment (MetroLivEn), Cosenza, Italy, 25–27 May 2022; pp. 48–53. [CrossRef]
32. Boutahir, M.K.; Farhaoui, Y.; Azrour, M.; Zeroual, I.; El Allaoui, A. Effect of Feature Selection on the Prediction of Direct Normal Irradiance. *Big Data Min. Anal.* **2022**, *5*, 309–317. [CrossRef]
33. Si, Z.; Yu, Y.; Yang, M.; Li, P. Hybrid Solar Forecasting Method Using Satellite Visible Images and Modified Convolutional Neural Networks. *IEEE Trans. Ind. Appl.* **2021**, *57*, 5–16. [CrossRef]
34. Marquez, R.; Pedro, H.T.; Coimbra, C.F. Hybrid solar forecasting method uses satellite imaging and ground telemetry as inputs to ANNs. *Sol. Energy* **2013**, *92*, 176–188. [CrossRef]
35. Aguiar, L.M.; Pereira, B.; Lauret, P.; Díaz, F.; David, M. Combining solar irradiance measurements, satellite-derived data and a numerical weather prediction model to improve intra-day solar forecasting. *Renew. Energy* **2016**, *97*, 599–610. [CrossRef]
36. Nonnenmacher, L.; Coimbra, C.F. Streamline-based method for intra-day solar forecasting through remote sensing. *Sol. Energy* **2014**, *108*, 447–459. [CrossRef]
37. Marchesoni-Acland, F.; Lauret, P.; Gomez, A.; Alonso-Suarez, R. Analysis of ARMA Solar Forecasting Models Using Ground Measurements and Satellite Images. In Proceedings of the 46th IEEE Photovoltaic Specialists Conference (PVSC), Chicago, IL, USA, 16–21 June 2019. [CrossRef]
38. Caldas, M.; Alonso-Suárez, R. Very short-term solar irradiance forecast using all-sky imaging and real-time irradiance measurements. *Renew. Energy* **2019**, *143*, 1643–1658. [CrossRef]
39. Schmidt, T.; Kalisch, J.; Lorenz, E.; Heinemann, D. Evaluating the spatio-temporal performance of sky-imager-based solar irradiance analysis and forecasts. *Atmos. Chem. Phys.* **2016**, *16*, 3399–3412. [CrossRef]
40. Nouri, B.; Kuhn, P.; Wilbert, S.; Prahl, C.; Pitz-Paal, R.; Blanc, P.; Schmidt, T.; Yasser, Z.; Santigosa, L.R.; Heineman, D. Nowcasting of DNI maps for the solar field based on voxel carving and individual 3D cloud objects from all sky images. *AIP Conf. Proc.* **2018**, *2033*, 190011. [CrossRef]
41. Blum, N.B.; Wilbert, S.; Nouri, B.; Lezaca, J.; Huckebrink, D.; Kazantzidis, A.; Heinemann, D.; Zarzalejo, L.F.; Jiménez, M.J.; Pitz-Paal, R. Measurement of diffuse and plane of array irradiance by a combination of a pyranometer and an all-sky imager. *Sol. Energy* **2022**, *232*, 232–247. [CrossRef]
42. Zhang, J.; Verschae, R.; Nobuhara, S.; Lalonde, J.-F. Deep photovoltaic nowcasting. *Sol. Energy* **2018**, *176*, 267–276. [CrossRef]
43. Chu, Y.; Pedro, H.T.C.; Nonnenmacher, L.; Inman, R.H.; Liao, Z.; Coimbra, C.F.M. A Smart Image-Based Cloud Detection System for Intrahour Solar Irradiance Forecasts. *J. Atmos. Ocean. Technol.* **2014**, *31*, 1995–2007. [CrossRef]
44. Sayeef, S.; West, S.R. Very short-term solar forecasting using inexpensive fisheye camera sky-imagery. In Proceedings of the 52nd Annual Conference of the Australian Solar Council, Melbourne, Australia, 8–9 May 2014.
45. Trigo-González, M.; Cortés-Carmona, M.; Marzo, A.; Alonso-Montesinos, J.; Martínez-Durbán, M.; López, G.; Portillo, C.; Batlles, F.J. Photovoltaic power electricity generation nowcasting combining sky camera images and learning supervised algorithms in the Southern Spain. *Renew. Energy* **2023**, *206*, 251–262. [CrossRef]
46. El-Amarty, N.; Marzouq, M.; El Fadili, H.; Bennani, S.D.; Ruano, A. A comprehensive review of solar irradiation estimation and forecasting using artificial neural networks: Data, models and trends. *Environ. Sci. Pollut. Res.* **2023**, *30*, 5407–5439. [CrossRef]
47. Chu, T.-P.; Guo, J.-H.; Leu, Y.-G.; Chou, L.-F. Estimation of solar irradiance and solar power based on all-sky images. *Sol. Energy* **2023**, *249*, 495–506. [CrossRef]
48. Paletta, Q.; Arbod, G.; Lasenby, J. Omnivision forecasting: Combining satellite and sky images for improved deterministic and probabilistic intra-hour solar energy predictions. *Appl. Energy* **2023**, *336*, 120818. [CrossRef]
49. Tiwari, S.; Sabzehgar, R.; Rasouli, M. Short Term Solar Irradiance Forecast Using Numerical Weather Prediction (NWP) with Gradient Boost Regression. In Proceedings of the 9th IEEE International Symposium on Power Electronics for Distributed Generation Systems (PEDG), Charlotte, NC, USA, 25–28 June 2018. [CrossRef]
50. Chaturvedi, D.K.; Isha, I. Solar Power Forecasting: A Review. *Int. J. Comput. Appl.* **2016**, *145*, 28–50. [CrossRef]
51. Lorenz, E.; Perez, R.; Remund, J. Comparison of Solar Radiation Forecasts for the USA. In Proceedings of the 23rd European Photovoltaic Solar Energy Conference, Valencia, Spain, 1–5 September 2008. [CrossRef]
52. Massidda, L.; Marrocu, M. Use of Multilinear Adaptive Regression Splines and numerical weather prediction to forecast the power output of a PV plant in Borkum, Germany. *Sol. Energy* **2017**, *146*, 141–149. [CrossRef]
53. Lopes, F.M.; Conceição, R.; Silva, H.G.; Salgado, R.; Collares-Pereira, M. Improved ECMWF forecasts of direct normal irradiance: A tool for better operational strategies in concentrating solar power plants. *Renew. Energy* **2021**, *163*, 755–771. [CrossRef]

54. Moon, S.-H.; Kim, Y.-H. Forecasting lightning around the Korean Peninsula by postprocessing ECMWF data using SVMs and undersampling. *Atmos. Res.* **2020**, *243*, 105026. [CrossRef]
55. Zamora, R.J.; Solomon, S.; Dutton, E.G.; Bao, J.W.; Trainer, M.; Portmann, R.W.; White, A.B.; Nelson, D.W.; McNider, R.T. Comparing MM5 radiative fluxes with observations gathered during the 1995 and 1999 Nashville southern oxidants studies. *J. Geophys. Res. Atmos.* **2003**, *108*, D2. [CrossRef]
56. Lara-Fanego, V.; Ruiz-Arias, J.; Pozo-Vázquez, D.; Santos-Alamillos, F.; Tovar-Pescador, J. Evaluation of the WRF model solar irradiance forecasts in Andalusia (southern Spain). *Sol. Energy* **2012**, *86*, 2200–2217. [CrossRef]
57. Huva, R.; Verbois, H.; Walsh, W. Comparisons of next-day solar forecasting for Singapore using 3DVAR and 4DVAR data assimilation approaches with the WRF model. *Renew. Energy* **2020**, *147*, 663–671. [CrossRef]
58. Dong, Z.; Yang, D.; Reindl, T.; Walsh, W.M. Satellite image analysis and a hybrid ESSS/ANN model to forecast solar irradiance in the tropics. *Energy Convers. Manag.* **2014**, *79*, 66–73. [CrossRef]
59. Mathiesen, P.; Collier, C.; Kleissl, J. A high-resolution, cloud-assimilating numerical weather prediction model for solar irradiance forecasting. *Sol. Energy* **2013**, *92*, 47–61. [CrossRef]
60. Thaker, J.; Höller, R.; Kapasi, M. Short-Term Solar Irradiance Prediction with a Hybrid Ensemble Model Using EUMETSAT Satellite Images. *Energies* **2024**, *17*, 329. [CrossRef]
61. Pierro, M.; De Felice, M.; Maggioni, E.; Moser, D.; Perotto, A.; Spada, F.; Cornaro, C. Data-driven upscaling methods for regional photovoltaic power estimation and forecast using satellite and numerical weather prediction data. *Sol. Energy* **2017**, *158*, 1026–1038. [CrossRef]
62. André, M.; Perez, R.; Soubdhan, T.; Schlemmer, J.; Calif, R.; Monjoly, S. Preliminary assessment of two spatio-temporal forecasting technics for hourly satellite-derived irradiance in a complex meteorological context. *Sol. Energy* **2019**, *177*, 703–712. [CrossRef]
63. Deo, R.C.; Şahin, M. Forecasting long-term global solar radiation with an ANN algorithm coupled with satellite-derived (MODIS) land surface temperature (LST) for regional locations in Queensland. *Renew. Sustain. Energy Rev.* **2017**, *72*, 828–848. [CrossRef]
64. Srivastava, S.; Lessmann, S. A comparative study of LSTM neural networks in forecasting day-ahead global horizontal irradiance with satellite data. *Sol. Energy* **2018**, *162*, 232–247. [CrossRef]
65. Deo, R.C.; Şahin, M.; Adamowski, J.F.; Mi, J. Universally deployable extreme learning machines integrated with remotely sensed MODIS satellite predictors over Australia to forecast global solar radiation: A new approach. *Renew. Sustain. Energy Rev.* **2019**, *104*, 235–261. [CrossRef]
66. Cros, S.; Sébastien, N.; Liandrat, O.; Schmutz, N. Cloud pattern prediction from geostationary meteorological satellite images for solar energy forecasting. *Soc. Photo Opt. Instrum. Eng. (SPIE)* **2014**, *9242*, 924202. [CrossRef]
67. Doorga, J.R.S.; Dhurmea, K.R.; Rughooputh, S.; Boojhawon, R. Forecasting mesoscale distribution of surface solar irradiation using a proposed hybrid approach combining satellite remote sensing and time series models. *Renew. Sustain. Energy Rev.* **2019**, *104*, 69–85. [CrossRef]
68. Kallio-Myers, V.; Riihelä, A.; Lahtinen, P.; Lindfors, A. Global horizontal irradiance forecast for Finland based on geostationary weather satellite data. *Sol. Energy* **2020**, *198*, 68–80. [CrossRef]
69. Kurzrock, F.; Cros, S.; Ming, F.C.; Otkin, J.A.; Hutt, A.; Linguet, L.; Lajoie, G.; Potthast, R. A Review of the Use of Geostationary Satellite Observations in Regional-Scale Models for Short-term Cloud Forecasting. *Meteorol. Z.* **2018**, *27*, 277–298. [CrossRef]
70. Lago, J.; De Brabandere, K.; De Ridder, F.; De Schutter, B. Short-term forecasting of solar irradiance without local telemetry: A generalized model using satellite data. *Sol. Energy* **2018**, *173*, 566–577. [CrossRef]
71. Mazorra Aguiar, L.; Pereira, B.; David, M.; Díaz, F.; Lauret, P. Use of satellite data to improve solar radiation forecasting with Bayesian Artificial Neural Networks. *Sol. Energy* **2015**, *122*, 1309–1324. [CrossRef]
72. Antuña-Sánchez, J.C.; Román, R.; Cachorro, V.E.; Toledano, C.; López, C.; González, R.; Mateos, D.; Calle, A.; de Frutos, Á.M. Relative sky radiance from multi-exposure all-sky camera images. *Atmos. Meas. Tech.* **2021**, *14*, 2201–2217. [CrossRef]
73. Schroedter-Homscheidt, M.; Gesell, G. Verification of sectoral cloud motion based direct normal irradiance nowcasting from satellite imagery. *AIP Conf. Proc.* **2016**, *1734*, 150007.
74. Markovics, D.; Mayer, M.J. Comparison of machine learning methods for photovoltaic power forecasting based on numerical weather prediction. *Renew. Sustain. Energy Rev.* **2022**, *161*, 112364. [CrossRef]
75. Rana, M.; Koprinska, I.; Agelidis, V.G. Univariate and multivariate methods for very short-term solar photovoltaic power forecasting. *Energy Convers. Manag.* **2016**, *121*, 380–390. [CrossRef]
76. Russo, M.; Leotta, G.; Pugliatti, P.; Gigliucci, G. Genetic programming for photovoltaic plant output forecasting. *Sol. Energy* **2014**, *105*, 264–273. [CrossRef]
77. Wang, Y.; Liu, D.; Xie, W.; Yang, M.; Gao, Z.; Ling, X.; Huang, Y.; Li, C.; Liu, Y.; Xia, Y. Day and Night Clouds Detection Using a Thermal-Infrared All-Sky-View Camera. *Remote Sens.* **2021**, *13*, 1852. [CrossRef]
78. Kuhn, P.; Garsche, D.; Wilbert, S.; Nouri, B.; Hanrieder, N.; Prahl, C.; Zarzarlejo, L.; Fernández, J.; Kazantzidis, A.; Schmidt, T.; et al. Shadow-camera based solar nowcasting system for shortest-term forecasts. *Meteorol. Z.* **2019**, *28*, 255–270. [CrossRef]
79. Wagdy, A.; Garcia-Hansen, V.; Isoardi, G.; Pham, K. A Parametric Method for Remapping and Calibrating Fisheye Images for Glare Analysis. *Buildings* **2019**, *9*, 219. [CrossRef]
80. Wei, J.; Li, C.-F.; Hu, S.-M.; Martin, R.R.; Tai, C.-L. Fisheye Video Correction. *IEEE Trans. Vis. Comput. Graph.* **2011**, *18*, 1771–1783. [CrossRef]

81. Bellas, N.; Chai, S.M.; Dwyer, M.; Linzmeier, D. Real-Time Fisheye Lens Distortion Correction Using Automatically Generated Streaming Accelerators. In Proceedings of the 2009 17th IEEE Symposium on Field Programmable Custom Computing Machines, Napa, CA, USA, 5–7 April 2009. [CrossRef]
82. Martínez-Chico, M.; Batlles, F.; Bosch, J. Cloud classification in a mediterranean location using radiation data and sky images. *Energy* **2011**, *36*, 4055–4062. [CrossRef]
83. Shields, J.E.; Karr, M.E.; Johnson, R.W.; Burden, A.R. Day/night whole sky imagers for 24-h cloud and sky assessment: History and overview. *Appl. Opt.* **2013**, *52*, 1605–1616. [CrossRef] [PubMed]
84. González, Y.; López, C.; Cuevas, E. Cloud nowcasting: Motion analysis of all sky images using velocity fields. In Proceedings of the 19th IMEKO TC4 Symposium Measurements of Electrical Quantities (Together with 17th TC4 IWADC Workshop on ADC and DAC Modelling and Testing), Barcelona, Spain, 18–19 July 2013.
85. Chu, Y.; Pedro, H.T.; Coimbra, C.F. Hybrid intra-hour DNI forecasts with sky image processing enhanced by stochastic learning. *Sol. Energy* **2013**, *98*, 592–603. [CrossRef]
86. Niccolai, A.; Nespoli, A. Sun Position Identification in Sky Images for Nowcasting Application. *Forecasting* **2020**, *2*, 488–504. [CrossRef]
87. Reno, M.J.; Hansen, C.W. Identification of periods of clear sky irradiance in time series of GHI measurements. *Renew. Energy* **2016**, *90*, 520–531. [CrossRef]
88. Kosch, M.J.; Pedersen, T.; Esposito, R. Wide angle mirror system design for distortionless imaging of the sky. *Appl. Opt.* **2009**, *48*, 4703–4708. [CrossRef]
89. Kuhn, P.; Nouri, B.; Wilbert, S.; Prahl, C.; Kozonek, N.; Schmidt, T.; Yasser, Z.; Ramirez, L.; Zarzalejo, L.; Meyer, A.; et al. Validation of an all-sky imager–based nowcasting system for industrial PV plants. *Prog. Photovolt. Res. Appl.* **2017**, *26*, 608–621. [CrossRef]
90. Kuhn, P.; Wilbert, S.; Schüler, D.; Prahl, C.; Haase, T.; Ramirez, L.; Zarzalejo, L.; Meyer, A.; Vuilleumier, L.; Blanc, P.; et al. Validation of spatially resolved all sky imager derived DNI nowcasts. In Proceedings of the SOLARPACES 2016: International Conference on Concentrating Solar Power and Chemical Energy Systems, Abu Dhabi, United Arab Emirates, 11–14 October 2016; AIP Publishing: Melville, NY, USA, 2017; Volume 1850, p. 1. [CrossRef]
91. West, S.R.; Rowe, D.; Sayeef, S.; Berry, A. Short-term irradiance forecasting using skycams: Motivation and development. *Sol. Energy* **2014**, *110*, 188–207. [CrossRef]
92. Yang, H.; Kurtz, B.; Nguyen, D.; Urquhart, B.; Chow, C.W.; Ghonima, M.; Kleissl, J. Solar irradiance forecasting using a ground-based sky imager developed at UC San Diego. *Sol. Energy* **2014**, *103*, 502–524. [CrossRef]
93. Huang, H.; Yoo, S.; Yu, D.; Huang, D.; Qin, H. Correlation and local feature based cloud motion estimation. In Proceedings of the MDMKDD '12: Proceedings of the Twelfth International Workshop on Multimedia Data Mining, Beijing, China, 12 August 2012. [CrossRef]
94. Chow, C.W.; Belongie, S.; Kleissl, J. Cloud motion and stability estimation for intra-hour solar forecasting. *Sol. Energy* **2015**, *115*, 645–655. [CrossRef]
95. Nguyen, D.A.; Kleissl, J. Stereographic methods for cloud base height determination using two sky imagers. *Sol. Energy* **2014**, *107*, 495–509. [CrossRef]
96. Costa-Surós, M.; Calbó, J.; González, J.; Martin-Vide, J. Behavior of cloud base height from ceilometer measurements. *Atmos. Res.* **2013**, *127*, 64–76. [CrossRef]
97. Kotthaus, S.; Grimmond, C.S.B. Atmospheric boundary-layer characteristics from ceilometer measurements. Part 1: A new method to track mixed layer height and classify clouds. *Q. J. R. Meteorol. Soc.* **2018**, *144*, 1525–1538. [CrossRef]
98. Nouri, B.; Wilbert, S.; Kuhn, P.; Hanrieder, N.; Schroedter-Homscheidt, M.; Kazantzidis, A.; Zarzalejo, L.; Blanc, P.; Kumar, S.; Goswami, N.; et al. Real-Time Uncertainty Specification of All Sky Imager Derived Irradiance Nowcasts. *Remote Sens.* **2019**, *11*, 1059. [CrossRef]
99. Richardson, W.; Krishnaswami, H.; Vega, R.; Cervantes, M. A Low Cost, Edge Computing, All-Sky Imager for Cloud Tracking and Intra-Hour Irradiance Forecasting. *Sustainability* **2017**, *9*, 482. [CrossRef]
100. Nouri, B.; Wilbert, S.; Segura, L.; Kuhn, P.; Hanrieder, N.; Kazantzidis, A.; Schmidt, T.; Zarzalejo, L.; Blanc, P.; Pitz-Paal, R. Determination of cloud transmittance for all sky imager based solar nowcasting. *Sol. Energy* **2019**, *181*, 251–263. [CrossRef]
101. Blanc, P.; Massip, P.; Kazantzidis, A.; Tzoumanikas, P.; Kuhn, P.; Wilbert, S.; Schüler, D.; Prahl, C. Short-term forecasting of high resolution local DNI maps with multiple fish-eye cameras in stereoscopic mode. *AIP Conf. Proc.* **2017**, *1850*, 140004. [CrossRef]
102. Peng, Z.; Yu, D.; Huang, D.; Heiser, J.; Yoo, S.; Kalb, P. 3D cloud detection and tracking system for solar forecast using multiple sky imagers. *Sol. Energy* **2015**, *118*, 496–519. [CrossRef]
103. Cheng, H.-Y. Hybrid solar irradiance now-casting by fusing Kalman filter and regressor. *Renew. Energy* **2016**, *91*, 434–441. [CrossRef]
104. Cheng, H.-Y.; Yu, C.-C. Solar irradiance now-casting with ramp-down event prediction via enhanced cloud detection and tracking. In Proceedings of the 2016 IEEE International Conference on Multimedia and Expo (ICME), Seattle, WA, USA, 11–15 July 2016. [CrossRef]
105. Cheng, H.-Y. Cloud tracking using clusters of feature points for accurate solar irradiance nowcasting. *Renew. Energy* **2017**, *104*, 281–289. [CrossRef]
106. Xie, W.; Wang, Y.; Xia, Y.; Gao, Z.; Liu, D. Angular Calibration of Visible and Infrared Binocular All-Sky-View Cameras Using Sun Positions. *Remote Sens.* **2021**, *13*, 2455. [CrossRef]

107. Román, R.; Antuña-Sánchez, J.C.; Cachorro, V.E.; Toledano, C.; Torres, B.; Mateos, D.; Fuertes, D.; López, C.; González, R.; Lapionok, T.; et al. Retrieval of aerosol properties using relative radiance measurements from an all-sky camera. *Atmos. Meas. Tech.* **2022**, *15*, 407–433. [CrossRef]
108. Chow, C.W.; Urquhart, B.; Lave, M.; Dominguez, A.; Kleissl, J.; Shields, J.; Washom, B. Intra-hour forecasting with a total sky imager at the UC San Diego solar energy testbed. *Sol. Energy* **2011**, *85*, 2881–2893. [CrossRef]
109. Palomares, M.; Bjerknes, V. La meteorología y la predicción del tiempo ¿Cuál es actualmente su nivel de fiabilidad?, ¿por qué se equivocan los meteorólogos? Available online: https://www.divulgameteo.es/uploads/Fiabilidad-predicci%C3%B3n.pdf (accessed on 18 May 2024).
110. Yang, D.; Dong, Z.; Reindl, T.; Jirutitijaroen, P.; Walsh, W.M. Solar irradiance forecasting using spatio-temporal empirical kriging and vector autoregressive models with parameter shrinkage. *Sol. Energy* **2014**, *103*, 550–562. [CrossRef]
111. Torres, J.F.; Troncoso, A.; Koprinska, I.; Wang, Z.; Martínez-Álvarez, F. Deep Learning for Big Data Time Series Forecasting Applied to Solar Power. In Proceedings of the 13th International Conference on Soft Computing Models in Industrial and Environmental Applications, San Sebastian, Spain, 6–8 June 2018. [CrossRef]
112. Singh, B.; Pozo, D. A Guide to Solar Power Forecasting using ARMA Models. In Proceedings of the 2019 IEEE PES Innovative Smart Grid Technologies Europe (ISGT-Europe), Bucharest, Romania, 29 September–2 October 2019. [CrossRef]
113. Bessa, R.; Trindade, A.; Silva, C.S.; Miranda, V. Probabilistic solar power forecasting in smart grids using distributed information. *Int. J. Electr. Power Energy Syst.* **2015**, *72*, 16–23. [CrossRef]
114. Li, Y.; Su, Y.; Shu, L. An ARMAX model for forecasting the power output of a grid connected photovoltaic system. *Renew. Energy* **2014**, *66*, 78–89. [CrossRef]
115. Alsharif, M.H.; Younes, M.K.; Kim, J. Time Series ARIMA Model for Prediction of Daily and Monthly Average Global Solar Radiation: The Case Study of Seoul, South Korea. *Symmetry* **2019**, *11*, 240. [CrossRef]
116. Kushwaha, V.; Pindoriya, N.M. Very short-term solar PV generation forecast using SARIMA model: A case study. In Proceedings of the 7th International Conference on Power Systems (ICPS), Pune, India, 21–23 December 2017. [CrossRef]
117. Gu, Y.; Wei, H.-L.; Boynton, R.J.; Walker, S.N.; Balikhin, M.A. Prediction of Kp index using NARMAX models with a robust model structure selection method. In Proceedings of the 9th International Conference on Electronics, Computers and Artificial Intelligence (ECAI), Targoviste, Romania, 29 June–1 July 2017. [CrossRef]
118. Pazikadin, A.R.; Rifai, D.; Ali, K.; Malik, M.Z.; Abdalla, A.N.; Faraj, M.A. Solar irradiance measurement instrumentation and power solar generation forecasting based on Artificial Neural Networks (ANN): A review of five years research trend. *Sci. Total. Environ.* **2020**, *715*, 136848. [CrossRef]
119. Yadav, A.K.; Chandel, S. Solar radiation prediction using Artificial Neural Network techniques: A review. *Renew. Sustain. Energy Rev.* **2014**, *33*, 772–781. [CrossRef]
120. Kamadinata, J.O.; Ken, T.L.; Suwa, T. Sky image-based solar irradiance prediction methodologies using artificial neural networks. *Renew. Energy* **2019**, *134*, 837–845. [CrossRef]
121. Wang, H.; Lei, Z.; Zhang, X.; Zhou, B.; Peng, J. A review of deep learning for renewable energy forecasting. *Energy Convers. Manag.* **2019**, *198*, 111799. [CrossRef]
122. Alkhayat, G.; Mehmood, R. A Review and Taxonomy of Wind and Solar Energy Forecasting Methods Based on Deep Learning. *Energy AI* **2021**, *4*, 100060. [CrossRef]
123. Shamshirband, S.; Rabczuk, T.; Chau, K.-W. A Survey of Deep Learning Techniques: Application in Wind and Solar Energy Resources. *IEEE Access* **2019**, *7*, 164650–164666. [CrossRef]
124. Hocaoglu, F.O.; Serttas, F. A novel hybrid (Mycielski-Markov) model for hourly solar radiation forecasting. *Renew. Energy* **2017**, *108*, 635–643. [CrossRef]
125. Wang, F.; Zhen, Z.; Wang, B.; Mi, Z. Comparative Study on KNN and SVM Based Weather Classification Models for Day Ahead Short Term Solar PV Power Forecasting. *Appl. Sci.* **2018**, *8*, 28. [CrossRef]
126. Liu, D.; Sun, K. Random forest solar power forecast based on classification optimization. *Energy* **2019**, *187*, 115940. [CrossRef]
127. Sobri, S.; Koohi-Kamali, S.; Rahim, N.A. Solar photovoltaic generation forecasting methods: A review. *Energy Convers. Manag.* **2018**, *156*, 459–497. [CrossRef]
128. David, M.; Luis, M.A.; Lauret, P. Comparison of intraday probabilistic forecasting of solar irradiance using only endogenous data. *Int. J. Forecast.* **2018**, *34*, 529–547. [CrossRef]
129. Boland, J. Spatial-temporal forecasting of solar radiation. *Renew. Energy* **2015**, *75*, 607–616. [CrossRef]
130. Huang, J.; Korolkiewicz, M.; Agrawal, M.; Boland, J. Forecasting solar radiation on an hourly time scale using a Coupled AutoRegressive and Dynamical System (CARDS) model. *Sol. Energy* **2012**, *87*, 136–149. [CrossRef]
131. Lauret, P.; Voyant, C.; Soubdhan, T.; David, M.; Poggi, P. A benchmarking of machine learning techniques for solar radiation forecasting in an insular context. *Sol. Energy* **2015**, *112*, 446–457. [CrossRef]
132. Monjoly, S.; André, M.; Calif, R.; Soubdhan, T. Hourly forecasting of global solar radiation based on multiscale decomposition methods: A hybrid approach. *Energy* **2017**, *119*, 288–298. [CrossRef]
133. Belmahdi, B.; Louzazni, M.; El Bouardi, A. One month-ahead forecasting of mean daily global solar radiation using time series models. *Optik* **2020**, *219*, 165207. [CrossRef]
134. Huang, C.; Wang, L.; Lai, L.L. Data-Driven Short-Term Solar Irradiance Forecasting Based on Information of Neighboring Sites. *IEEE Trans. Ind. Electron.* **2018**, *66*, 9918–9927. [CrossRef]

135. Muhammad, A.; Gaya, M.S.; Aliyu, R.; Abdulkadir, R.A.; Umar, I.D.; Yusuf, L.A.; Ali, M.U.; Khairi, M. Forecasting of global solar radiation using anfis and armax techniques. *IOP Conf. Ser. Mater. Sci. Eng.* **2018**, *303*, 012016. [CrossRef]
136. Dewangan, C.L.; Singh, S.N.; Chakrabarti, S. Solar irradiance forecasting using wavelet neural network. In Proceedings of the 2017 IEEE PES Asia-Pacific Power and Energy Engineering Conference (APPEEC), Bangalore, India, 8–10 November 2017. [CrossRef]
137. Babu, M.K.; Ray, P. A Wavelet Neural Network Model for Hourly Solar Radiation Forecasting from Daily Solar Radiation. In Proceedings of the IEEE 5th International Conference for Convergence in Technology (I2CT), Bombay, India, 29–31 March 2019. [CrossRef]
138. Sharma, V.; Yang, D.; Walsh, W.; Reindl, T. Short term solar irradiance forecasting using a mixed wavelet neural network. *Renew. Energy* **2016**, *90*, 481–492. [CrossRef]
139. Shakya, A.; Michael, S.; Saunders, C.; Armstrong, D.; Pandey, P.; Chalise, S.; Tonkoski, R. Solar Irradiance Forecasting in Remote Microgrids Using Markov Switching Model. *IEEE Trans. Sustain. Energy* **2017**, *8*, 895–905. [CrossRef]
140. Rai, A.; Shrivastava, A.; Jana, K.C. A robust auto encoder-gated recurrent unit (AE-GRU) based deep learning approach for short term solar power forecasting. *Optik* **2021**, *252*, 168515. [CrossRef]
141. Ghimire, S.; Deo, R.C.; Raj, N.; Mi, J. Deep solar radiation forecasting with convolutional neural network and long short-term memory network algorithms. *Appl. Energy* **2019**, *253*, 113541. [CrossRef]
142. Qin, J.; Jiang, H.; Lu, N.; Yao, L.; Zhou, C. Enhancing solar PV output forecast by integrating ground and satellite observations with deep learning. *Renew. Sustain. Energy Rev.* **2022**, *167*, 112680. [CrossRef]
143. Gao, Y.; Miyata, S.; Akashi, Y. Interpretable deep learning models for hourly solar radiation prediction based on graph neural network and attention. *Appl. Energy* **2022**, *321*, 119288. [CrossRef]
144. Ospina, J.; Newaz, A.; Faruque, M.O. Forecasting of PV plant output using hybrid wavelet-based LSTM-DNN structure model. *IET Renew. Power Gener.* **2019**, *13*, 1087–1095. [CrossRef]
145. Mustaqeem; Ishaq, M.; Kwon, S. A CNN-Assisted deep echo state network using multiple Time-Scale dynamic learning reservoirs for generating Short-Term solar energy forecasting. *Sustain. Energy Technol. Assess.* **2022**, *52*, 102275. [CrossRef]
146. Gensler, A.; Henze, J.; Sick, B.; Raabe, N. Deep Learning for solar power forecasting—An approach using AutoEncoder and LSTM Neural Networks. In Proceedings of the 2016 IEEE International Conference, Systems, Man, and Cybernetics (SMC), Budapest, Hungary, 9 October 2016. [CrossRef]
147. Bouzgou, H.; Gueymard, C.A. Minimum redundancy—Maximum relevance with extreme learning machines for global solar radiation forecasting: Toward an optimized dimensionality reduction for solar time series. *Sol. Energy* **2017**, *158*, 595–609. [CrossRef]
148. Zhen, Z.; Liu, J.; Zhang, Z.; Wang, F.; Chai, H.; Yu, Y.; Lu, X.; Wang, T.; Lin, Y. Deep Learning Based Surface Irradiance Mapping Model for Solar PV Power Forecasting Using Sky Image. *IEEE Trans. Ind. Appl.* **2020**, *56*, 3385–3396. [CrossRef]
149. Sun, Y.C.; Venugopal, V.; Brandt, A.R. Short-term solar power forecast with deep learning: Exploring optimal input and output configuration. *Sol. Energy* **2019**, *188*, 730–741. [CrossRef]
150. Ghimire, S.; Deo, R.C.; Casillas-Pérez, D.; Salcedo-Sanz, S. Boosting solar radiation predictions with global climate models, observational predictors and hybrid deep-machine learning algorithms. *Appl. Energy* **2022**, *316*, 119063. [CrossRef]
151. Moncada, A.; Richardson, W.; Vega-Avila, R. Deep Learning to Forecast Solar Irradiance Using a Six-Month UTSA SkyImager Dataset. *Energies* **2018**, *11*, 1988. [CrossRef]
152. Ağbulut, U.; Gürel, A.E.; Biçen, Y. Prediction of daily global solar radiation using different machine learning algorithms: Evaluation and comparison. *Renew. Sustain. Energy Rev.* **2020**, *135*, 110114. [CrossRef]
153. Voyant, C.; Notton, G.; Kalogirou, S.; Nivet, M.-L.; Paoli, C.; Motte, F.; Fouilloy, A. Machine learning methods for solar radiation forecasting: A review. *Renew. Energy* **2017**, *105*, 569–582. [CrossRef]
154. Pedro, H.T.; Coimbra, C.F.; David, M.; Lauret, P. Assessment of machine learning techniques for deterministic and probabilistic intra-hour solar forecasts. *Renew. Energy* **2018**, *123*, 191–203. [CrossRef]
155. Benali, L.; Notton, G.; Fouilloy, A.; Voyant, C.; Dizene, R. Solar radiation forecasting using artificial neural network and random forest methods: Application to normal beam, horizontal diffuse and global components. *Renew. Energy* **2018**, *132*, 871–884. [CrossRef]
156. Mejia, J.F.; Giordano, M.; Wilcox, E. Conditional summertime day-ahead solar irradiance forecast. *Sol. Energy* **2018**, *163*, 610–622. [CrossRef]
157. Lopes, F.M.; Silva, H.G.; Salgado, R.; Cavaco, A.; Canhoto, P.; Collares-Pereira, M. Short-term forecasts of GHI and DNI for solar energy systems operation: Assessment of the ECMWF integrated forecasting system in southern Portugal. *Sol. Energy* **2018**, *170*, 14–30. [CrossRef]
158. Schroedter-Homscheidt, M.; Benedetti, A.; Killius, N. Verification of ECMWF and ECMWF/MACC's global and direct irradiance forecasts with respect to solar electricity production forecasts. *Meteorol. Z.* **2017**, *26*, 1–19. [CrossRef]
159. Arbizu-Barrena, C.; Ruiz-Arias, J.A.; Rodríguez-Benítez, F.J.; Pozo-Vázquez, D.; Tovar-Pescador, J. Short-term solar radiation forecasting by advecting and diffusing MSG cloud index. *Sol. Energy* **2017**, *155*, 1092–1103. [CrossRef]
160. Iversen, E.B.; Morales, J.M.; Møller, J.K.; Madsen, H. Probabilistic forecasts of solar irradiance using stochastic differential equations. *Environmetrics* **2014**, *25*, 152–164. [CrossRef]

161. Lima, F.J.L.; Martins, F.R.; Pereira, E.B.; Lorenz, E.; Heinemann, D. Forecast for surface solar irradiance at the Brazilian Northeastern region using NWP model and artificial neural networks. *Renew. Energy* **2016**, *87 Pt 1*, 807–818. [CrossRef]
162. Verbois, H.; Huva, R.; Rusydi, A.; Walsh, W. Solar irradiance forecasting in the tropics using numerical weather prediction and statistical learning. *Sol. Energy* **2018**, *162*, 265–277. [CrossRef]
163. Zhang, Y.; Shen, Y.; Xia, X.; Shi, G. Validation of GFS day-ahead solar irradiance forecasts in China. *arXiv* **2020**, arXiv:2007.01639. [CrossRef]
164. Pereira, S.; Canhoto, P.; Salgado, R.; Costa, M.J. Development of an ANN based corrective algorithm of the operational ECMWF global horizontal irradiation forecasts. *Sol. Energy* **2019**, *185*, 387–405. [CrossRef]
165. Eseye, A.T.; Zhang, J.; Zheng, D. Short-term photovoltaic solar power forecasting using a hybrid Wavelet-PSO-SVM model based on SCADA and Meteorological information. *Renew. Energy* **2018**, *118*, 357–367. [CrossRef]
166. Huang, J.; Rikus, L.J.; Qin, Y.; Katzfey, J. Assessing model performance of daily solar irradiance forecasts over Australia. *Sol. Energy* **2018**, *176*, 615–626. [CrossRef]
167. Perez, R.; Schlemmer, J.; Hemker, K.; Kivalov, S.; Kankiewicz, A.; Dise, J. Solar energy forecast validation for extended areas & economic impact of forecast accuracy. In Proceedings of the 2016 IEEE 43rd Photovoltaic Specialists Conference (PVSC), Portland, OR, USA, 5–10 June 2016. [CrossRef]
168. Yang, H.; Kleissl, J. Preprocessing WRF initial conditions for coastal stratocumulus forecasting. *Sol. Energy* **2016**, *133*, 180–193. [CrossRef]
169. Jang, H.S.; Bae, K.Y.; Park, H.; Sung, D.K. Solar Power Prediction Based on Satellite Images and Support Vector Machine. *IEEE Trans. Sustain. Energy* **2016**, *7*, 1255–1263. [CrossRef]
170. Miller, S.D.; Rogers, M.A.; Haynes, J.M.; Sengupta, M.; Heidinger, A.K. Short-term solar irradiance forecasting via satellite/model coupling. *Sol. Energy* **2018**, *168*, 102–117. [CrossRef]
171. Wang, P.; van Westrhenen, R.; Meirink, J.F.; van der Veen, S.; Knap, W. Surface solar radiation forecasts by advecting cloud physical properties derived from Meteosat Second Generation observations. *Sol. Energy* **2018**, *177*, 47–58. [CrossRef]
172. Ahn, H.; Yu, J.; Yeom, J.-M. Deep Learning based Prediction of Solar Surface Irradiance with Geostationary Satellite Images. In Proceedings of the 2022 17th Annual System of Systems Engineering Conference (SOSE), Rochester, NY, USA, 7–11 June 2022; pp. 311–315. [CrossRef]
173. Alonso-Montesinos, J.; Batlles, F.; Bosch, J. Beam, diffuse and global solar irradiance estimation with satellite imagery. *Energy Convers. Manag.* **2015**, *105*, 1205–1212. [CrossRef]
174. Su, Y.; Li, N.; Yang, H.; Wang, F.; Sun, C.; Zhen, Z.; Zou, Z.; Ge, X. A Feature Importance Analysis Based Solar Irradiance Mapping Model Using Multi-channel Satellite Remote Sensing Data. In Proceedings of the 2022 IEEE/IAS 58th Industrial and Commercial Power Systems Technical Conference (I&CPS), Las Vegas, NV, USA, 2–5 May 2022; pp. 1–9. [CrossRef]
175. Cros, S.; Badosa, J.; Szantaï, A.; Haeffelin, M. Reliability Predictors for Solar Irradiance Satellite-Based Forecast. *Energies* **2020**, *13*, 5566. [CrossRef]
176. Kim, C.K.; Kim, H.-G.; Kang, Y.-H.; Yun, C.-Y. Toward Improved Solar Irradiance Forecasts: Comparison of the Global Horizontal Irradiances Derived from the COMS Satellite Imagery Over the Korean Peninsula. *Pure Appl. Geophys.* **2017**, *174*, 2773–2792. [CrossRef]
177. Amillo, A.G.; Huld, T.; Müller, R. A New Database of Global and Direct Solar Radiation Using the Eastern Meteosat Satellite, Models and Validation. *Remote Sens.* **2014**, *6*, 8165–8189. [CrossRef]
178. Hess, M.; Koepke, P.; Schult, I. Optical Properties of Aerosols and Clouds: The Software Package OPAC. *Bull. Am. Meteorol. Soc.* **1998**, *79*, 831–844. [CrossRef]
179. Ineichen, P.; Perez, R. A new airmass independent formulation for the Linke turbidity coefficient. *Sol. Energy* **2002**, *73*, 151–157. [CrossRef]
180. Jayadevan, V.T.; Rodriguez, J.J.; Cronin, A.D. A New Contrast-Enhancing Feature for Cloud Detection in Ground-Based Sky Images. *J. Atmos. Ocean. Technol.* **2015**, *32*, 209–219. [CrossRef]
181. Heinle, A.; Macke, A.; Srivastav, A. Automatic cloud classification of whole sky images. *Atmos. Meas. Tech.* **2010**, *3*, 557–567. [CrossRef]
182. Souza-Echer, M.P.; Pereira, E.B.; Bins, L.S.; Andrade, M.A.R. A Simple Method for the Assessment of the Cloud Cover State in High-Latitude Regions by a Ground-Based Digital Camera. *J. Atmos. Ocean. Technol.* **2006**, *23*, 437–447. [CrossRef]
183. Long, C.N.; Sabburg, J.M.; Calbó, J.; Pagès, D. Retrieving Cloud Characteristics from Ground-Based Daytime Color All-Sky Images. *J. Atmos. Ocean. Technol.* **2006**, *23*, 633–652. [CrossRef]
184. Kazantzidis, A.; Tzoumanikas, P.; Bais, A.; Fotopoulos, S.; Economou, G. Cloud detection and classification with the use of whole-sky ground-based images. *Atmos. Res.* **2012**, *113*, 80–88. [CrossRef]
185. Yang, J.; Lu, W.; Ma, Y.; Yao, W. An Automated Cirrus Cloud Detection Method for a Ground-Based Cloud Image. *J. Atmos. Ocean. Technol.* **2012**, *29*, 527–537. [CrossRef]
186. Neto, S.L.M.; von Wangenheim, A.; Pereira, E.B.; Comunello, E. The Use of Euclidean Geometric Distance on RGB Color Space for the Classification of Sky and Cloud Patterns. *J. Atmos. Ocean. Technol.* **2010**, *27*, 1504–1517. [CrossRef]
187. Li, Q.; Lu, W.; Yang, J. A hybrid thresholding algorithm for Cloud Detection on Ground-Based Color Images. *J. Atmos. Ocean. Technol.* **2011**, *28*, 1286–1296. [CrossRef]

188. Ghonima, M.S.; Urquhart, B.; Chow, C.W.; Shields, J.E.; Cazorla, A.; Kleissl, J. A method for cloud detection and opacity classification based on ground based sky imagery. *Atmos. Meas. Tech.* **2012**, *5*, 2881–2892. [CrossRef]
189. Shields, J.E.; Karr, M.E.; Tooman, T.P.; Sowle, D.H.; Moore, S.T. The whole sky imager—A year of progress. In Proceedings of the Eighth Atmospheric Radiation Measurement (ARM) Science Team Meeting, Tucson, Arizona, 23–27 March 1998; pp. 1–9.
190. Liria, J.; Kozonek, N.; Ferrera, F.; Valenzuela, R.; Zarzalejo, L.; Ramirez, L.; Garcia, G.; Prahl, C.; Nouri, B.; Wilbert, S. Application of Whole Sky Imagers for Data Selection for Radiometer Calibration. In Proceedings of the EU PVSEC, Munich, Germany, 20–24 June 2016; pp. 1493–1498. [CrossRef]
191. Taravat, A.; Del Frate, F.; Cornaro, C.; Vergari, S. Neural Networks and Support Vector Machine Algorithms for Automatic Cloud Classification of Whole-Sky Ground-Based Images. *IEEE Geosci. Remote Sens. Lett.* **2014**, *12*, 666–670. [CrossRef]
192. Xia, M.; Lu, W.; Yang, J.; Ma, Y.; Yao, W.; Zheng, Z. A hybrid method based on extreme learning machine and k-nearest neighbor for cloud classification of ground-based visible cloud image. *Neurocomputing* **2015**, *160*, 238–249. [CrossRef]
193. Ye, L.; Cao, Z.; Xiao, Y. DeepCloud: Ground-Based Cloud Image Categorization Using Deep Convolutional Features. *IEEE Trans. Geosci. Remote Sens.* **2017**, *55*, 5729–5740. [CrossRef]
194. Otsu, N. A threshold selection method from gray-level histograms. *IEEE Trans. Syst. Man Cybern.* **1979**, *9*, 62–66. [CrossRef]
195. Pawar, P.; Cortés, C.; Murray, K.; Kleissl, J. Detecting clear sky images. *Sol. Energy* **2019**, *183*, 50–56. [CrossRef]
196. Seiz, G.; Shields, J.; Feister, U.; Baltsavias, E.P.; Gruen, A. Cloud mapping with ground-based photogrammetric cameras. *Int. J. Remote Sens.* **2007**, *28*, 2001–2032. [CrossRef]
197. Calbó, J.; Long, C.N.; González, J.-A.; Augustine, J.; McComiskey, A. The thin border between cloud and aerosol: Sensitivity of several ground based observation techniques. *Atmos. Res.* **2017**, *196*, 248–260. [CrossRef]
198. Quaas, J.; Stevens, B.; Stier, P.; Lohmann, U. Interpreting the cloud cover—Aerosol optical depth relationship found in satellite data using a general circulation model. *Atmos. Chem. Phys.* **2010**, *10*, 6129–6135. [CrossRef]
199. Liu, Z.; Vaughan, M.A.; Winker, D.M.; Hostetler, C.A.; Poole, L.R.; Hlavka, D.; Hart, W.; McGill, M. Use of probability distribution functions for discriminating between cloud and aerosol in lidar backscatter data. *J. Geophys. Res. Atmos.* **2004**, *109*, D15202. [CrossRef]
200. Sassen, K.; Wang, Z. The Clouds of the Middle Troposphere: Composition, Radiative Impact, and Global Distribution. *Surv. Geophys.* **2011**, *33*, 677–691. [CrossRef]
201. Kahn, B.H.; Chahine, M.T.; Stephens, G.L.; Mace, G.G.; Marchand, R.T.; Wang, Z.; Barnet, C.D.; Eldering, A.; Holz, R.E.; Kuehn, R.E.; et al. Cloud type comparisons of AIRS, CloudSat, and CALIPSO cloud height and amount. *Atmos. Meas. Tech.* **2008**, *8*, 1231–1248. [CrossRef]
202. Kratzke, N.; Quint, P.-C. Understanding cloud-native applications after 10 years of cloud computing—A systematic mapping study. *J. Syst. Softw.* **2017**, *126*, 1–16. [CrossRef]
203. Chen, T.; Rossow, W.B.; Zhang, Y. Radiative Effects of Cloud-Type Variations. *J. Clim.* **2000**, *13*, 264–286. [CrossRef]
204. Kokhanovsky, A. Optical properties of terrestrial clouds. *Earth Sci. Rev.* **2004**, *64*, 189–241. [CrossRef]
205. Lohmann, U.; Neubauer, D. The importance of mixed-phase and ice clouds for climate sensitivity in the global aerosol–climate model ECHAM6-HAM2. *Atmos. Chem. Phys.* **2018**, *18*, 8807–8828. [CrossRef]
206. Chang, F.; Li, Z. Estimating the vertical variation of cloud droplet effective radius using multispectral near-infrared satellite measurements. *J. Geophys. Res. Atmos.* **2002**, *107*, AAC 7-1–AAC 7-12. [CrossRef]
207. Tapakis, R.; Charalambides, A. Equipment and methodologies for cloud detection and classification: A review. *Sol. Energy* **2013**, *95*, 392–430. [CrossRef]
208. Liu, L.; Sun, X.; Chen, F.; Zhao, S.; Gao, T. Cloud Classification Based on Structure Features of Infrared Images. *J. Atmos. Ocean. Technol.* **2011**, *28*, 410–417. [CrossRef]
209. Wang, F.; Xuan, Z.; Zhen, Z.; Li, Y.; Li, K.; Zhao, L.; Shafie-Khah, M.; Catalão, J.P. A minutely solar irradiance forecasting method based on real-time sky image-irradiance mapping model. *Energy Convers. Manag.* **2020**, *220*, 113075. [CrossRef]
210. Singh, M.; Glennen, M. Automated ground-based cloud recognition. *Pattern Anal. Appl.* **2005**, *8*, 258–271. [CrossRef]
211. Zhang, J.; Liu, P.; Zhang, F.; Song, Q. CloudNet: Ground-Based Cloud Classification with Deep Convolutional Neural Network. *Geophys. Res. Lett.* **2018**, *45*, 8665–8672. [CrossRef]
212. Bernecker, D.; Riess, C.; Angelopoulou, E.; Hornegger, J. *Towards Improving Solar Irradiance Forecasts with Methods from Computer Vision*; University of Erlangen-Nuremberg: Nuremberg, Germany, 2012.
213. Thirion, J.-P. Image matching as a diffusion process: An analogy with Maxwell's demons. *Med. Image Anal.* **1998**, *2*, 243–260. [CrossRef] [PubMed]
214. Fischer, B.; Modersitzki, J. Curvature Based Image Registration. *J. Math. Imaging Vis.* **2003**, *18*, 81–85. [CrossRef]
215. Wood-Bradley, P.; Zapata, J.; Pye, J. Cloud tracking with optical flow for short-term solar forecasting. In Proceedings of the 50th Conference of the Australian Solar Energy Society, Melbourne, Australia, 2–7 November 2012.
216. Lucas, B.D.; Kanade, T. An iterative image registration technique with an application to stereo vision. In Proceedings of the DARPA Image Understanding Workshop, Pittsburgh, PA, USA, 24 August 1981; pp. 121–130.
217. Li, W.; Zhang, F.; Lin, H.; Chen, X.; Li, J.; Han, W. Cloud Detection and Classification Algorithms for Himawari-8 Imager Measurements Based on Deep Learning. *IEEE Trans. Geosci. Remote Sens.* **2022**, *60*, 4107117. [CrossRef]
218. Zhen, Z.; Xuan, Z.; Wang, F.; Sun, R.; Duić, N.; Jin, T. Image phase shift invariance based multi-transform-fusion method for cloud motion displacement calculation using sky images. *Energy Convers. Manag.* **2019**, *197*, 111853. [CrossRef]

219. Cros, S.; Liandrat, O.; Sebastien, N.; Schmutz, N. Extracting cloud motion vectors from satellite images for solar power forecasting. In Proceedings of the International Geoscience and Remote Sensing Symposium (IGARSS), Quebec City, QC, Canada, 13–18 July 2014. [CrossRef]
220. Marquez, R.; Coimbra, C.F. Intra-hour DNI forecasting based on cloud tracking image analysis. *Sol. Energy* **2013**, *91*, 327–336. [CrossRef]